

Simplifying BRDF Acquisition

Shubham Chitnis

Dual Degree Project report for
Interdisciplinary dual degree program (IDDDP) in
Centre for Machine Intelligence and Data Science (C-MInDS)

Under the supervision of

Professor Sharat Chandran



Indian Institute of Technology Bombay
Powai, 400076

ABSTRACT

Light interactions, modeled using the bidirectional reflectance distribution function (BRDF), form a basis for how objects appear to us. Conventionally, BRDFs are captured through rigorous and time-consuming measurements. Rendering the materials then becomes a task of looking up the right value from the tabulated measurements. This approach becomes difficult with more complex materials requiring denser measurements and more storage. Parametric models ease things up by allowing for a means to represent materials compactly. This helps ease up the rendering, but the acquisition step still poses a challenge. More efficient means to capture material BRDFs help speed up the acquisition process.

In this work, we suggest using in-plane angle pairs for material capture. We show them to be able to capture important BRDF trends for isotropic materials through our experiments. To demonstrate this, we use existing physics-based and network-based parametric models and perform comparisons between the entire gamut of data and our suggested subset.

Additionally, we propose an MLP network to learn BRDFs in the spectral domain. This provides a means to have a compact BRDF model while staying in the spectral domain, avoiding any premature wavelength compression. Finally, we study the performance of these methods as a function of the number of samples used for fitting. This helps us answer the question of how little data is sufficient to represent a material BRDF accurately in the subset of materials considered.

ACKNOWLEDGEMENTS

This project was a culmination of the direct or indirect help and guidance of several individuals. I would like to take this opportunity to extend my gratitude to all of them.

First and foremost, I would like to thank my supervisor, Professor Sharat Chandran, for his continuous support and expertise, which has been invaluable not just in academics but otherwise too. Right from believing in my abilities and allowing me to work under his supervision to spending countless hours solving my queries and brainstorming alongside me. I believe our regular *touch bases* helped the project immensely, and the dual degree project experience has made me better equipped to handle my doctoral journey.

I would also like to thank Professor Aditya Sole from the Color Lab, NTNU. Throughout the course of my project, his inputs were very helpful and I wouldn't hesitate to call him my unofficial co-guide. My visit to their campus also taught me a lot. Also, many thanks to Professor Parag Chaudhuri for attending my defense in the first stage. His courses on Computer Graphics and Image Synthesis helped me build a solid base and further appreciate the field.

Last but not the least, I would like to thank my family, my parents, grandparents, friends, and my pet Thor. They have been a place of joy during stressful times. Their support meant a lot and the project would not have been where it's currently at without them.

HONOR CODE

I, *Shubham Chitnis, 190020033* declare that this written submission represents my ideas in my own words, and where others' ideas or words have been included, I have adequately cited and referenced the original sources. I declare that I have properly and accurately acknowledged all sources used in the production of this report. I also declare that I have adhered to all principles of academic honesty and integrity and have not misrepresented, fabricated, or falsified any idea/data/fact/source in my submission. I understand that any violation of the above will be a cause for disciplinary action by the Institute and can also evoke penal action from the sources that have thus not been properly cited or from whom proper permission has not been taken when needed.

Contents

Abstract	2
Acknowledgements	3
Honor code	4
1 Introduction	7
1.1 Motivation	8
1.2 Problem description	9
1.3 Contributions	10
1.4 Scope	10
2 Background and Related work	12
2.1 Background	12
2.1.1 BRDF data preprocessing	12
2.2 Spectral compression	13
2.2.1 ABC parametric model	14
2.2.2 Neural layered BRDFs	16
2.3 Related work	17
3 Dataset	19
3.1 MERL data	19
3.2 Packaging materials	20
4 Tristimulus representation	22
4.1 Parametric model	22
4.1.1 Data fitting	23
4.1.2 Data parameterization	24
4.1.3 Results	25
4.2 Neural latent space	28
4.2.1 Results	29
5 Spectral representation	33
5.1 MLP model	33
5.1.1 Network training	34

5.1.2	Results	35
6	Ablation studies	37
6.1	ABC method	37
6.2	NLB method	40
7	Conclusion and future work	44
	References	46
	Appendices	50

Chapter 1

Introduction

Capturing realistic material appearance has been a long-standing goal of graphics research. Efforts are being put into coming up with better ways to capture and render real-world materials. This requires us to study how light interacts with these materials, forming the basis of how any object appears to us. This is where the term BRDF, meaning bidirectional reflectance distribution function, comes into the picture. BRDF is a physical property that captures how much of the light coming from a particular direction gets reflected in some other direction. These directions are often called the incident (or incoming) direction and the reflected (or outgoing) direction. A more sophisticated definition of the BRDF comes from Nicodemus et al.[1] as given in Equation 1.1.

$$f_{\lambda}(\omega_i, \omega_r) = \frac{dL_r(\omega_r)}{dE_i(\omega_i)} = \frac{dL_r(\omega_r)}{L_i(\omega_i) \cos \theta_i d\omega_i} \quad (1.1)$$

Here, f_{λ} is the BRDF, a function of the wavelength being considered. ω_i and ω_r are the incoming and outgoing directions respectively. θ_i is the angle between the surface normal and incoming direction. dE_i is the differential incoming irradiance, and dL_o is the reflected differential outgoing radiance. It is possible to further split the incoming irradiance into the product of the incoming radiance and projected differential solid angle.

Measuring material BRDFs allows us to render them in arbitrary scenes. This is crucial if we wish to create an accurate digital copy of some real-world material. This approach is not only used in entertainment media such as movies and games but also has wide applications in areas like architecture, design, and packaging,

where visual inspection is key for making informed decisions.

1.1 Motivation

Sophisticated measurement setups are available to capture material light interactions, but solely capturing them is not enough, as not only is this approach highly material-specific, but also rendering such vast data poses storage issues. A way around this was presented in the form of analytical models. These models were compact and involved parameters that were estimated using the measured data. The parameters also allowed users to control the behavior of the resulting BRDF, making it possible to generate synthetic materials.

Starting from a simple constant, progressively more accurate and complex parametric BRDF models were proposed in the literature [2]. This was necessary to be able to model most of the global phenomena surrounding the materials (reflections, refractions, iridescence, translucence, etc.). This included a class of models based on the microfacet theory proposed by Cook and Torrance [3] (see Section 2.2.1). Recent progress in deep learning also motivated works using neural networks. Unlike parametric models, networks aren't bound to the underlying physics, making them, in principle, more expressive and capable of representing a broader class of materials. This comes at the cost of the need for additional data because of the data-hungry nature of neural networks and a lack of prior as was the case with physics-based parametric models.

Even though increasingly accurate models were built, the amount of measurements required to capture certain optical phenomena increased, and so did the time required for taking measurements and calibrating these setups. It was stated that even the most recent approaches took 2-3 days to measure anisotropic sample BRDFs [4]. This calls for the need to have more efficient representations that require far fewer measurements to capture the full gamut of possible material light interactions.

Additionally, it is common to see tristimulus RGB data being used in exist-

ing BRDF and rendering works, but this data often lacks details compared to the spectral domain. The reason being that tristimulus theory restricts us to a subset of the entire color gamut, resulting in loss of information. To our knowledge compact representations are not proposed specific to the spectral domain. However, they can provide a way to compactly represent BRDFs in the spectral domain and avoid wavelength compression down to RGB.

1.2 Problem description

There are two separate problems at large. First, we need ways to speed up the data acquisition process since it is time-consuming. This can be done using more efficient representations that learn from less data or by cleverly choosing more informative data samples. Second, with a majority of the existing representations being in the RGB domain, any spectral data needs to be compressed for it to be suitable to learn. This causes us to lose out on available information for the sole purpose of data fitting. Proposing representations in the spectral domain might help solve this problem.

For isotropic materials, we show that using in-plane measurements, a small subset of the possible incoming and outgoing direction pairs, we can generate powerful representations and maintain visual fidelity during 3d renderings. These results are obtained for materials with diverse reflectance properties, ranging from simple diffuse and specular to materials showing goniochromatism, that is, varying chromaticity (color) based on the direction from which we are viewing.

In-plane measurements are those in which the incoming and outgoing directions are restricted to form a plane along with the surface normal instead of freely moving around the hemisphere. Solely using in-plane measurements, however, is not sufficient for 3d renderings as casted rays can very well be out-of-plane, but the fitted parametric representations offer a way to render them. We further test the ability of our representations by progressively reducing the number of data points used for model fitting. This study addresses an important question: how

little data can we use to capture all the underlying BRDF trends faithfully?

1.3 Contributions

Summarizing, we can point out the main contributions of this project:

- We use in-plane data to fit existing parametric models and neural networks, demonstrating that a more conservative acquisition of BRDF data should be enough for accurate representation in the RGB domain.
- We propose an MLP network for representing material BRDFs in the spectral domain, hence avoiding the need to perform a wavelength compression.
- We progressively reduce the fitting dataset to test the representation ability of proposed models.
- A custom rendering loop was written for the Neural layered BRDF models (see Section A.1) using Mitsuba 3 [5].

1.4 Scope

It is important to clarify the goals of our work. The aim of this report is not to propose new parametric models for learning BRDFs. We use existing work from the literature, most notably, the ABC model by Low et al. [6] and the NLB network by Fan et al. [7]. The only model that we *propose* is for the spectral domain, where there aren't many existing representations. The architecture of this *model* is not novel, and there are similar works suggesting approaches, both physics and network-based. In fact, our work is, for the most part, independent of the choice of model. Our focus lies in the amount of fitting data these models use. Existing works often use the full spectrum of the available data and fail to address the lengthy acquisition process. We suggest the use of in-plane angles for model fitting and demonstrate our results support this claim, thereby reducing the number of acquisition steps required.

The structure of the report is as follows. Sections 2.1 and 2.3 discuss essential prerequisites and related literature before heading into our approach. In Chapter 3, we describe two data capture processes for the publicly available MERL dataset [8] and a separate spectral dataset of four packaging print materials. In Chapters 4 and 5, we deal with the RGB and spectral domain respectively, suggesting means to learn material representations and analyze the quality of reconstruction. We perform ablation studies in Chapter 6 and conclude with a brief summary followed by the limitations of our method and possible future work.

Chapter 2

Background and Related work

2.1 Background

We need to cover some groundwork on how the raw data gets processed into useful BRDF values for fitting. A wavelength compression step is also covered, which helps us compress our spectral data down to the tristimulus domain. Furthermore, before going over our method, it is important to understand the ABC microfacet parametric model introduced by Low et al. [6] since we use it as the basis of our approach. Similarly, we will go over the work on neural layered BRDFs by Fan et al. [7] as we use their representation network to learn material encodings.

2.1.1 BRDF data preprocessing

The packaging print materials come from a study in Norway performed by Sole et al. [9]. Their apparatus, Murakami's GCMS-3B goniospectrophotometer (GCMS for brevity), outputs a biconical reflectance instead of the BRDF. This can be defined as a ratio of the outgoing to the incoming flux (See Equation 2.1).

$$\beta(2\pi \rightarrow 2\pi) = \frac{\int_{\Omega_r} L_r \cos \theta_r d\omega_r}{\int_{\Omega_i} L_i \cos \theta_i d\omega_i} \quad (2.1)$$

Here, θ_r and θ_i represent the angle between the outgoing and incoming rays with the surface normal (not to be confused with ω , which is the solid angle). This step is essential as BRDF values often tend to be extremely high in magnitude. This is due to there being no theoretical upper bound to their range. So, to get the BRDF values, a calibration step is performed (see Equation 2.2).

$$\frac{f_{\text{sample}}}{f_{\text{PFD}}} = \frac{\beta_{\text{sample}}}{\beta_{\text{PRD}}} \quad (2.2)$$

PRD is a perfect reflecting diffuse surface with a BRDF value of $\frac{1}{\pi}$. Instead of a PRD surface, we use the Munsell white N9 sheet, which is assumed to have a reflectivity 79% that of a PRD [10]. The Munsell sample is measured in GCMS along with our other materials (see Section 3.2). Thus, the modified BRDF equation becomes:

$$f \approx \frac{0.79}{\pi} \frac{\beta_{\text{sample}}}{\beta_{\text{Munsell}}} \quad (2.3)$$

The output BRDF acts as a ground truth for any further model fitting.

2.2 Spectral compression

Scene renderings generate an RGB output. More often than not, this makes it necessary to compress spectral BRDF data into its tristimulus equivalent prior to rendering. This compression step from the spectral domain leads to information loss but is nevertheless an important precursor to model fitting and rendering. Our measurement setup generates BRDF data for 31 wavelengths spanning the wavelength range of 400-700nm. Moving to the sRGB domain requires us to pass through the XYZ domain. The XYZ space is a CIE standard color space based on human perception that captures the entire spectral gamut using its three primaries: X, Y, and Z. Given a wavelength spectrum, the CIE standard observer color-matching functions are used to perform a dot product (see Equation 2.4), transforming BRDF values appropriately in the XYZ space (see [11] for more).

$$X_{\text{GCMS}} = k \sum_{\lambda=400\text{nm}}^{700\text{nm}} f_{\lambda} E_{\lambda}(i) \bar{x}_{\lambda}$$

$$k = \frac{100}{\sum_{\lambda=400\text{nm}}^{700\text{nm}} E_{\lambda}(i) \bar{y}_{\lambda}} \quad (2.4)$$

\bar{x}_{λ} , \bar{y}_{λ} and \bar{z}_{λ} are the color matching functions. f_{λ} is the measured spectral

BRDF, k is a normalizing factor, and $E(i)$ is an estimate of the illuminant spectral power distribution (SPD). In this work, we use the standard D65 illuminant SPD (see Figure 2.1). Equations for Y_{GCMS} and Z_{GCMS} similarly use \bar{y} and \bar{z} respectively. The XYZ also allows us to separate chromaticity from luminance and handle normalization while keeping color information intact. Moving from the XYZ space to the sRGB space is a straightforward matrix multiplication [12].

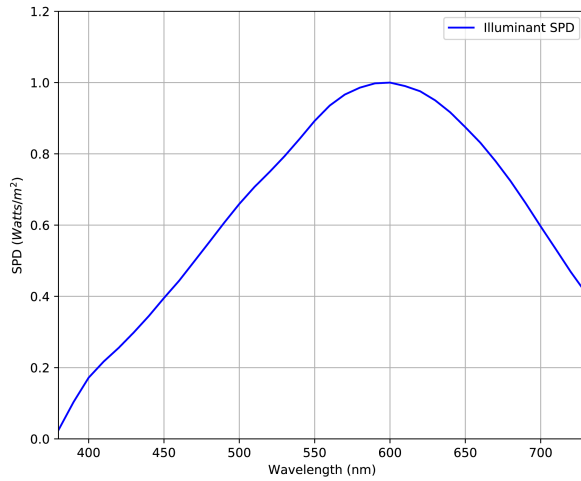


Figure 2.1: Spectral power distribution (SPD) of the D65 standard illuminant.

2.2.1 ABC parametric model

The ABC parametric model is a derivative of the microfacet theory based Cook-Torrance model [3]. Microfacet theory represents the surface (macrosurface) as a chain of segments (microsurfaces) that behave like perfect mirrors, with their surface normals following a probability distribution D . In their work, Low et al. [6] proposed the ABC distribution for surface normals and demonstrated its ability to accurately model various materials while still being compact (9 parameters).

The BRDF is defined as in Equation 2.5.

$$f(\omega_i, \omega_r) = k_d + \frac{F(\theta_h)G(\mathbf{n} \cdot \omega_i, \mathbf{n} \cdot \omega_r)D(\sqrt{1 - (\mathbf{n} \cdot \mathbf{h})})}{\pi (\mathbf{n} \cdot \omega_i)(\mathbf{n} \cdot \omega_r)} \quad (2.5)$$

Here, θ_h is the angle between the surface normal \mathbf{n} and the halfway vector \mathbf{h} . k_d denotes the diffuse albedo, the term responsible for modulating channel-

wise diffuse reflection component. F is the classic Fresnel factor handling the amount of surface reflectance and transmittance. It should be noted that surface transmittance is defined for surfaces that allow light to pass through them. For opaque objects, this transmittance component gets absorbed into the material. F is defined in Equation 2.6. Also, surface normals introduce areas where the light gets masked or shadowed. To compensate for this, a geometric attenuation factor G is introduced (in Equation 2.7).

$$F = \frac{(g - c)^2}{2(g + c)^2} \left\{ 1 + \frac{[c(g + c) - 1]^2}{[c(g - c) + 1]^2} \right\} \quad (2.6)$$

$$G = \min \left\{ 1, \frac{2(\mathbf{n} \cdot \mathbf{h})(\mathbf{n} \cdot \omega_r)}{(\omega_r \cdot \mathbf{h})}, \frac{2(\mathbf{n} \cdot \mathbf{h})(\mathbf{n} \cdot \omega_i)}{(\omega_r \cdot \mathbf{h})} \right\} \quad (2.7)$$

In Equation (2.6), $c = \omega_r \cdot \mathbf{h}$, $g = \eta^2 + c^2 - 1$ and η is the index of refraction. D , as stated earlier, is the ABC-based micro-facet distribution given in Equation (2.8).

$$S(f) = \frac{A}{(1 + Bf^2)^C}, \quad (2.8)$$

ABC distribution accounts for specular component with the A parameter. Similarly, B and C decide on the width of the specular peaks and the fall-off rate of wide-angle scattering. Figure 2.2 shows the effect of changing these parameters.

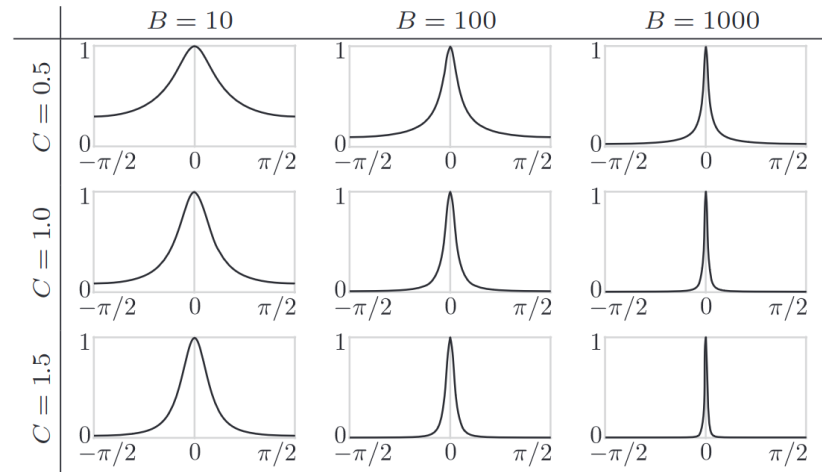


Figure 2.2: $S(f)$ plots for varying values of B and C . Figure from Low et al. [6]

2.2.2 Neural layered BRDFs

Several works have involved neural networks to learn material BRDFs and BTFs (bidirectional texture function) [13, 14, 7, 15, 16, 17]. Fan et al. [7] addresses the challenge of rendering layered materials (polished metals, fabrics, etc.) with their neural network framework Neural layered BRDFs (NLB). With the majority of existing layered BRDF solutions for rendering demonstrating high variance and/or being compute-intensive, the authors think of describing materials in the latent space. A representation network is trained to simultaneously learn the material latent space and BRDF trends for those materials.

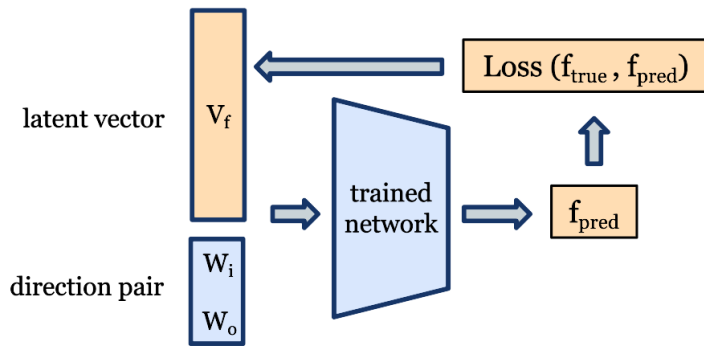


Figure 2.3: Schematic for the NLB network.

This approach is useful because, unlike other network-based methods, their network is material-agnostic, and once it is trained, we just need to backpropagate over the trained network to retrieve the latent vector (V). An overview of this is shown in Figure 2.3. The operation can be represented as in Equation 2.9. Here g_1 is the representation operator. ω_i and ω_r are the incoming and outgoing directions in the Euclidean space, and $f(\omega_i, \omega_r)$ is the BRDF measurement for the stated directions.

$$g_1(\omega_i, \omega_r, V) = f(\omega_i, \omega_r) \quad (2.9)$$

The authors also deal with material layering, but our pipeline doesn't require it, so any further details regarding that are added in Appendix A. Given a latent vector, it is possible to use a renderer such as Mitsuba [5] and query the network for BRDF values during rendering.

2.3 Related work

BRDF measurements, representation, and rendering are fields of active research. This work focuses primarily on suggesting representations and rendering methods for in-plane BRDF measurements for isotropic materials and benchmarking performance of existing works on the same. We won't be describing measurement setups other than the ones that were part of our data collection process (in Section 3). Although using the measurement data as is, like a lookup table, leads to highly accurate BRDF values, it leads to storage issues very soon, especially with more complex materials like anisotropic or spatially varying ones. This can be mitigated by using analytical models that approximate BRDFs through physics-based derivations or cleverly chosen functions. A survey of such models can be found in [2]. Although useful, parametric models lack flexibility due to being restricted to the underlying theory.

It was possible for neural networks to learn repeating patterns in the BRDF data and make highly accurate predictions on a wide range of materials. Sztrajman et al. [14] demonstrate the ability of networks to model both isotropic and anisotropic materials compactly. Latent representations were also learned for ease in BRDF editing and interpolation. Liu et al. [18] use meta-learning to efficiently pick measurement directions for learning BRDFs. While these works lie in the tabular BRDF domain, the DeepBRDF method by Hu et al. [13] learns to translate the domain from images (spherical material with environmental map lighting) to tabular BRDF data and back. This also allows for material extraction from scene images. While early methods trained material-specific networks, Fan et al. [7] use a joint latent vector and network weight optimization to get a common BRDF representation network (as discussed in Section 2.2.2).

Although Fan et al. can handle spatially varying BRDF maps by generating a latent texture map, specific works targeting spatially varying (SV)BRDFs and bidirectional texture functions (BTFs) have been proposed. SVBRDF literature consists mainly of normal, diffuse, and specular maps retrieval from rendered

material images [19, 20]. This includes both planar materials and otherwise, in which case additional geometric information is also estimated with depth maps. This allows for downstream tasks such as material relighting [21], although, as shown by [22], relighting can be done without getting the BRDF maps. Similarly, BTF data can be dealt with using encoder-decoder architectures [15, 16], with more sophisticated neural representations using multi-resolution [17] or bi-plane neural textures [23] for efficient and accurate representation and rendering.

Chapter 3

Dataset

In this chapter, we discuss the datasets used along with their measurement setups for retrieving BRDFs. The two sources for BRDF data are the materials from the well-known MERL dataset [8] and packaging print materials from a study in Norway [9]. Figure 3.1 shows a preview of the BRDF values for materials from both datasets. A schematic of the packaging print materials' measuring setup is provided in Figure 3.2(a)

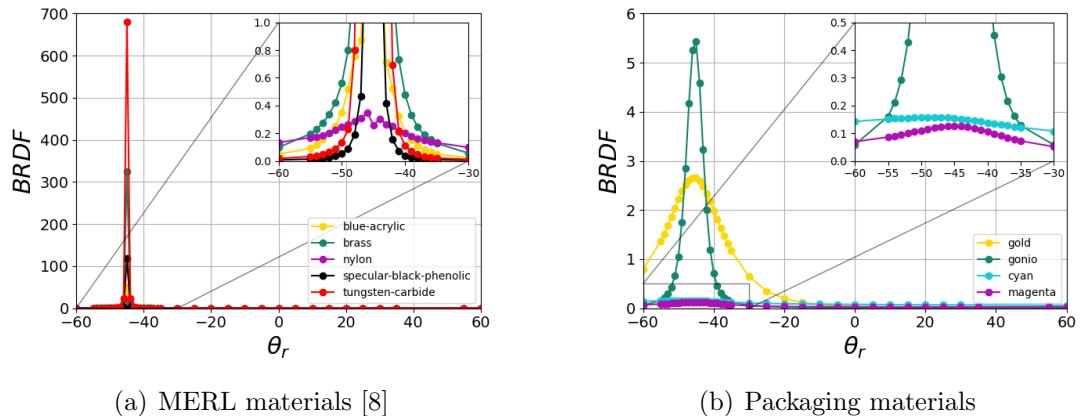


Figure 3.1: Bidirectional reflectance (f) measured at 560nm for an incoming angle $\theta_i = -45^\circ$ and various outgoing angles θ_r .

3.1 MERL data

There are 100+ isotropic material BRDFs in MERL. The measurements are carried out by an RGB camera through multiple high dynamic range (HDR) images of the spherical materials. The material to be measured is loaded onto a turntable arrangement, and the camera is rotated around to produce 20-80 million data points (each pixel is a separate measurement). This setup takes around three

hours for every sample, followed by a noise removal step. Unlike our dataset, these measurements are not restricted to being in-plane. This allows for richer data at the cost of more time and storage.

We consider five MERL materials: Tungsten carbide, Nylon, Brass, Blue acrylic, and Specular black phenolic. Figure 3.1(a) shows the variation between their reflectance values. This dataset is essential for us to confirm our hypothesis that in-plane measurements are representative of the overall optical properties in the case of isotropic materials. By artificially starving the MERL dataset to in-plane angles, we can make comparisons with the full gamut of possible directions (further details in Chapter 4).

3.2 Packaging materials

There are four packaging print materials primarily used in our study: Gold, Gonio, Cyan, and Magenta. All of them are isotropic, with Gold and Gonio showing a highly specular nature, whereas the rest being majorly diffuse, as seen from Figure 3.1(b). Additionally, Gonio is a greenish-blue sample showing goniochromaticity, which was touched upon in Section 1.2. Figure 3.2(b) demonstrates the varying chromaticity for different angle configurations.

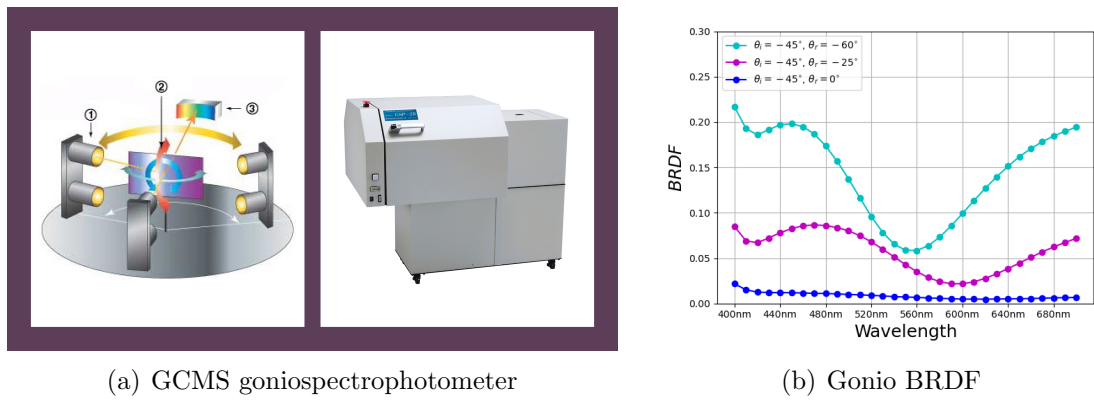


Figure 3.2: (Left) The GCMS goniospectrophotometer prototype [<https://www.mcrl.co.jp>]. (Right) For the same incoming angle (-45°), depending on the outgoing angle (-60° , -25° and 0°), the measured spectral BRDF can be vastly different.

The acquisition process is different from MERL. A planar sample of the mate-

rial is placed on the device, and a tungsten halogen bulb is used to illuminate the material surface. An array of silicon photo-diodes act as light sensors to capture the reflection off of the material surface. The material can be rotated through angles $\pm 80^\circ$ with respect to the incident light source, and GCMS outputs the spectral radiance factor for the wavelengths 390nm - 730nm with a 10nm interval. The preprocessing steps outlined in Section 2.1.1 are followed to obtain the material BRDF.

Chapter 4

Tristimulus representation

It is imperative to generate tristimulus BRDF data, as most modern-day rendering softwares either only support RGB data or perform heuristics to convert any spectral data into RGB for rendering. With our packaging dataset being in the spectral domain, we follow a commonly used approach to tone map its 31 wavelengths down to RGB using tristimulus color theory (see Section 2.2). We suggest using the ABC parametric model stated in Section 2.2.1 to represent BRDF data compactly. Similarly, instead of using a physics-based model, one can also turn to neural networks with strong priors built into them through extensive training. This step is also essential as in-plane measurements aren't enough for performing 3D renderings by themselves. Generating BRDF parameters or latent vectors through an optimization step ensures that we eventually reach an optimum that is still a strong approximation of the actual material nature.

4.1 Parametric model

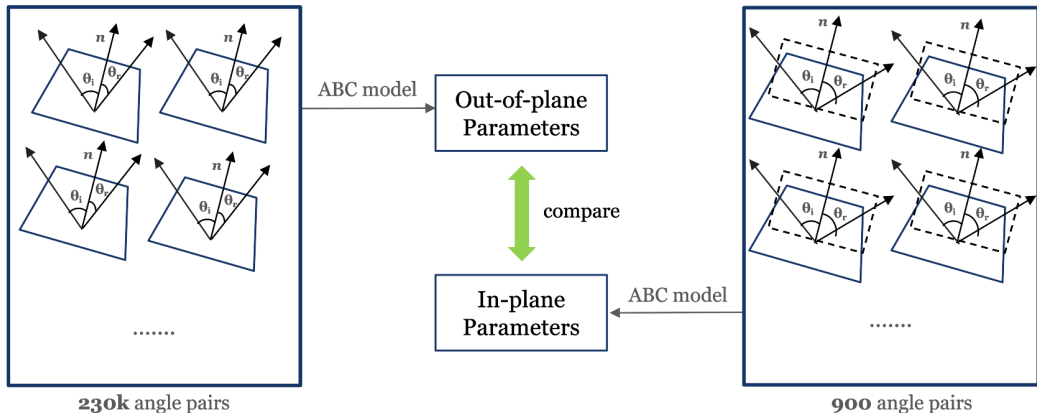


Figure 4.1: Schematic for our in-plane vs out-of-plane fitting pipeline using the ABC microfacet model.

The ABC microfacet model [6] demonstrates highly accurate results for MERL materials. This result, however, is when we consider a total of 28,800 outgoing angles per incident direction, which approximates to a total of 230k samples. From a data acquisition point of view, these many measurements often require multiple hours. We suggest using in-plane measurements, which are a tiny subset of what was considered earlier. For isotropic materials, in particular, our study shows that parameters fitted on the in-plane data generated visually comparable renderings. This would enable us to take around 256x less data, thus saving time. Overview provided in Figure 4.1.

4.1.1 Data fitting

With our packaging print materials, we only take in-plane measurements using the GCMS (Section 3.2), but an additional study is performed where we use materials from the MERL dataset. This allows us to compare how in-plane angles fare against the full gamut of measurements used by Low et al. [6].

Our data-fitting pipeline strongly resembles the one used by Low et al. There are nine parameters in total, of which six are optimized and three are estimated directly. The equation to be optimized is the same as Equation 2.5. But for ease of understanding, a modified Equation 4.1 is provided.

$$f(\omega_i, \omega_o) = \frac{k_{d_{\text{rgb}}}}{\pi} + \frac{F(\theta_h)G(\mathbf{n} \cdot \omega_i, \mathbf{n} \cdot \omega_o)D_{\text{rgb}}(\sqrt{1 - (\mathbf{n} \cdot \mathbf{h})})}{(\mathbf{n} \cdot \omega_i)(\mathbf{n} \cdot \omega_o)} \quad (4.1)$$

The parameters are $k_{d_{\text{rgb}}}$, A_{rgb} , B , C , and η . $k_{d_{\text{rgb}}}$ denotes the channel-wise diffuse component albedo, and A_{rgb} is the channel-wise scaling parameter present in D_{rgb} , the modified ABC distribution. We estimate the $k_{d_{\text{rgb}}}$ term by taking channel-wise BRDF minimum and multiplying it by π . This is because the specular term is non-negative and diminishes the farther we are from the specular region, meaning that the lowest BRDF value for a channel should be k_d/π . For the other parameters, we perform a least squares optimization similar to [6]. The estimates obtained by this approach are more accurate than performing an op-

Dataset	θ_i interval	θ_r interval: Diffuse	θ_r interval: Glossy
DS1	5°	5°	1°

Table 4.1: Angle intervals used for the in-plane subset of MERL. Both θ_i and θ_r range from -60° to 60° .

timizing over all the parameters. ABC model output is highly sensitive to the diffuse albedo. We believe that the lack of data during optimization leads to suboptimal albedo estimates, leading to erroneous BRDF values.

The choice of loss function has a big influence on the BRDF reconstruction. We reviewed early works experimenting with various loss functions [24, 25, 6] and chose Equation 4.2. There, f_{mea} is the measured, and f_{pred} is the estimated material BRDF. θ_i and θ_r are incident (incoming) and reflected (outgoing) angles, respectively. The logarithmic term gives more visually accurate results.

$$L_{\text{cus}} = \frac{1}{N} \sum_{n=1}^N (g_{\text{mea}} - g_{\text{pred}})^2 \sin \theta_r$$

$$g_{\text{mea}} = \ln(1 + \cos \theta_i f_{\text{mea}})$$

$$g_{\text{pred}} = \ln(1 + \cos \theta_i f_{\text{pred}}) \quad (4.2)$$

4.1.2 Data parameterization

We consider angles from Table 4.1 for fitting the ABC model. We measure them for the packaging print samples, but with MERL materials, we specifically have to restrict the entire data to the mentioned angles for fair comparison.

Another point of difference between the packaging materials and MERL materials is the parameterization. Being in-plane, packaging materials are parameterized with just the incoming and outgoing angles with the surface normal. On the other hand, MERL materials need both polar angles (θ and ϕ) for every incoming and outgoing direction. This forces us to make a choice as to what the azimuthal angles ϕ_i and ϕ_r should be. We pick the incoming azimuthal angle ϕ_i as 0° , whereas the outgoing azimuthal angle is either 0° or 180° , depending on

whether both the directions lie on the same or opposite side of the normal. For isotropic materials especially, the parameterization will hold true even if we pick a different incoming azimuthal angle, as long as the outgoing direction lies in its plane with the surface normal.

4.1.3 Results

Following the data fitting pipeline, we end up with the nine BRDF parameters. To test out our method, we produce three kinds of results.

We assign the BRDF parameters to an object in a 3D scene and use Mitsuba [5] to generate renderings. This is a material preview scene with the material of interest applied onto a helmet-like mesh. The plugin used implements the ABC model and an importance sampling routine. It is part of the Microfacet BRDF library built by Jonathan Dupuy. For MERL materials, we also have a point of comparison from Low et al. material BRDF estimates (using 256x more data). A side-by-side comparison of the two, as shown in Figure 4.2, ascertains that in-plane estimates maintain visual fidelity with less data. We also provide renderings for our packaging materials in Figure 4.3. Furthermore, instead of restricting ourselves to rendering a single material, we render the "Modern Living Room" scene provided in the Mitsuba 3 gallery. A static page is hosted where we provide a side-by-side comparison of three renderings: using tabular MERL data, using ABC parameters estimated with Low et al. angles, and finally, parameters estimated with in-plane angles. The page can be found here <https://shubham3008.github.io/living-room-compare>.

Other than the renderings, we provide visual plots where we track measured BRDFs alongside their parametric estimates. This comparison is more useful to understand the quality of fits at a finer level. Figures 4.4 and 4.5 show these visual plots for MERL and packaging materials, respectively.

Finally, we also produce relative-rmse error plots (see Equation 4.3).

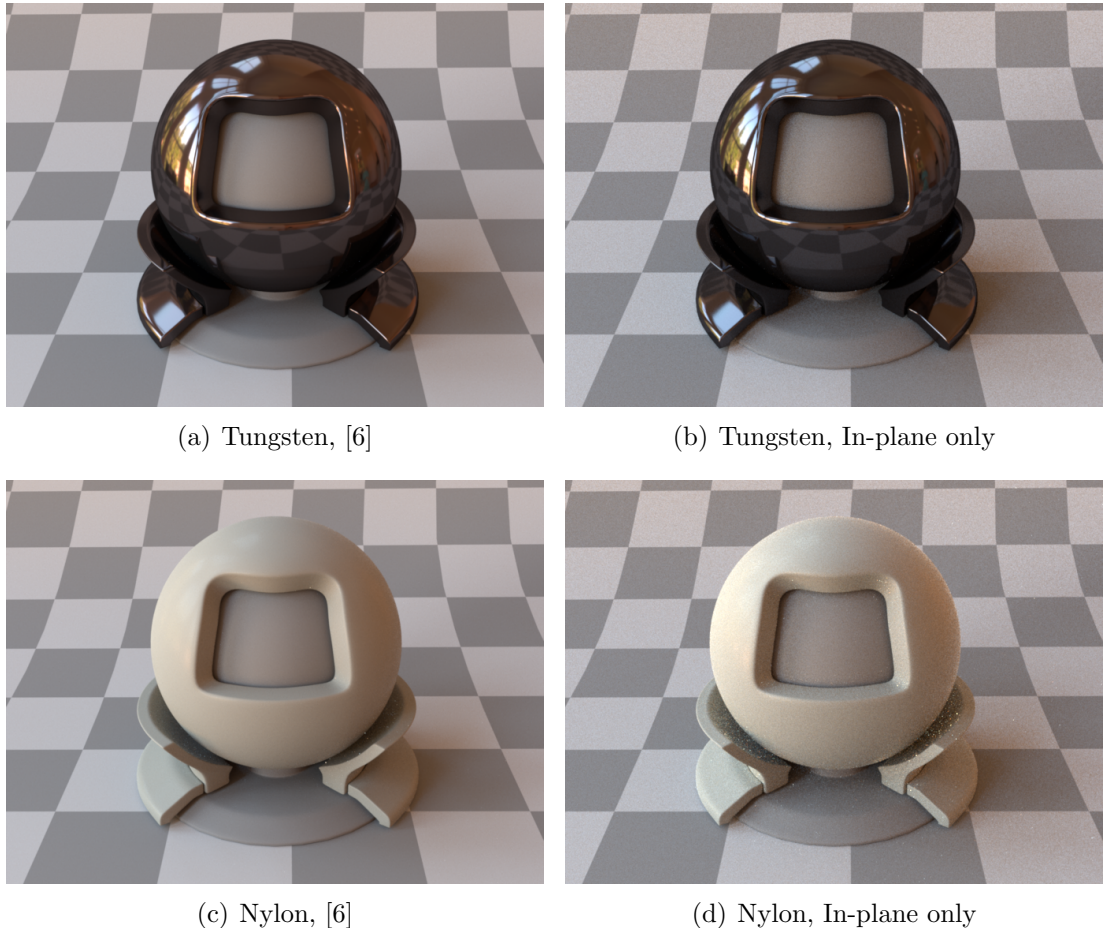


Figure 4.2: Scene renderings for visual comparison. Our first result is that rendering with in-plane data (900 samples, right) viewed in isolation is excellent. Further, when viewed comparatively, the results are almost indistinguishable from the one in [6] (230400 samples, left).

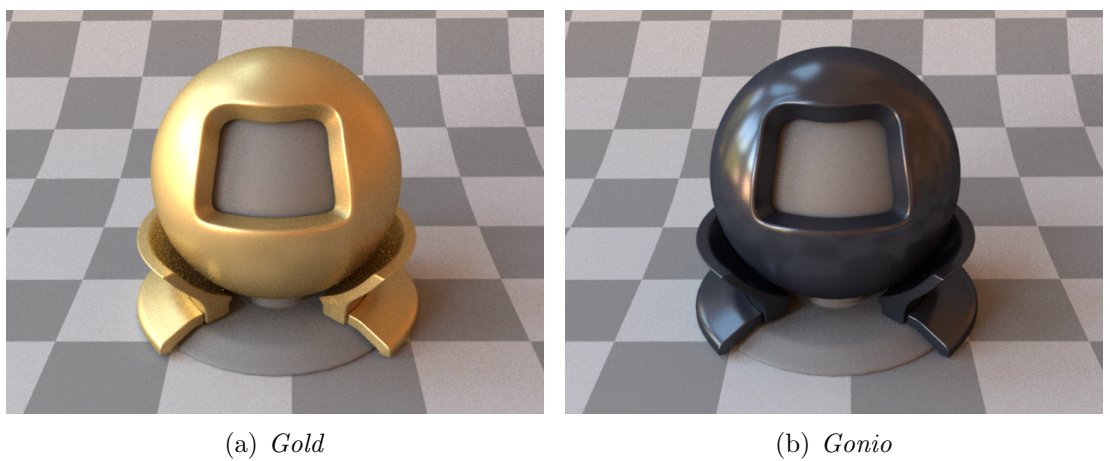
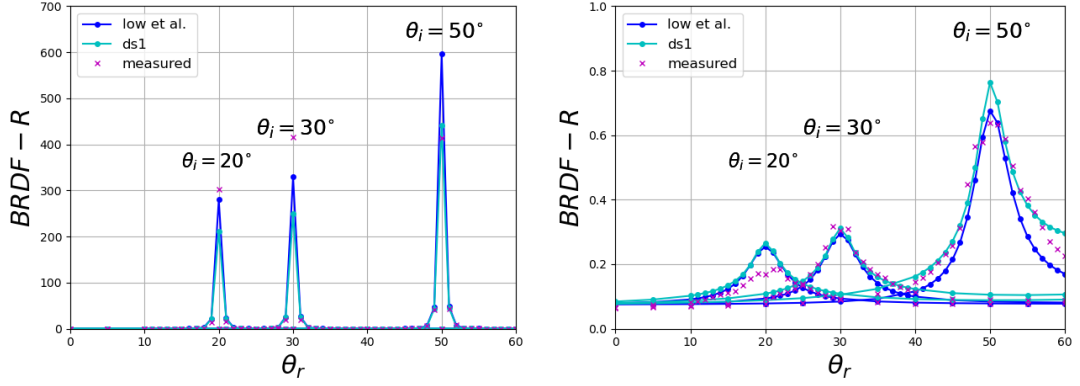


Figure 4.3: Scene renderings for our packaging print materials, *Gold* and *Gonio*. These renderings are for in-plane data with only 900 samples.



(a) Tungsten, Red Channel

(b) Nylon, Red Channel

Figure 4.4: BRDF of MERL materials calculated with only in-plane data estimates compared to the estimates from [6] compared to the actual measurements.

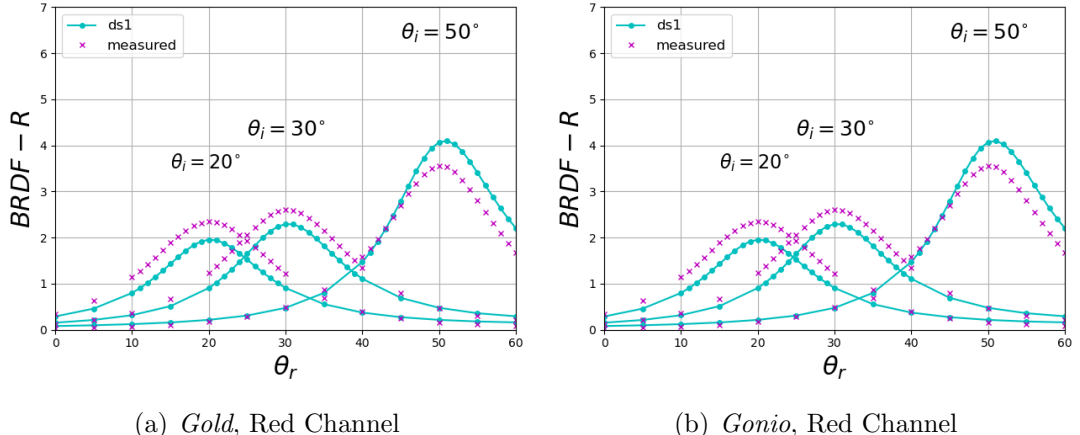


Figure 4.5: Contrasting fitted data with measured BRDF data of two packaging print materials.

$$L_{\text{rel-rmse}} = \sqrt{\frac{1}{N} \sum_{n=1}^N \left(\frac{f_{\text{pred}} - f_{\text{mea}}}{f_{\text{mea}}} \right)^2} \quad (4.3)$$

The error is calculated only for the glossy region as it contributes more towards the fit quality. Also, we average the error out over the three channels to get an overall loss. Figure 4.6 shows the error for various incoming angles for the MERL materials. The error here is comparable to the Low et al. estimates. We similarly provide error plots for our packaging materials in Figure 4.7.

For the packaging materials, our obtained parameters are able to accurately estimate BRDFs in both diffuse and specular regions. MERL materials with steep

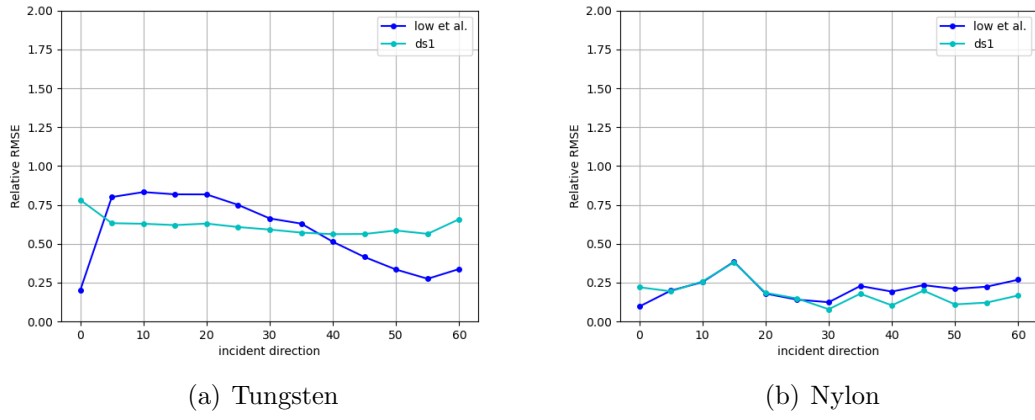


Figure 4.6: Relative RMSE errors as a function of incoming angle for two MERL materials.

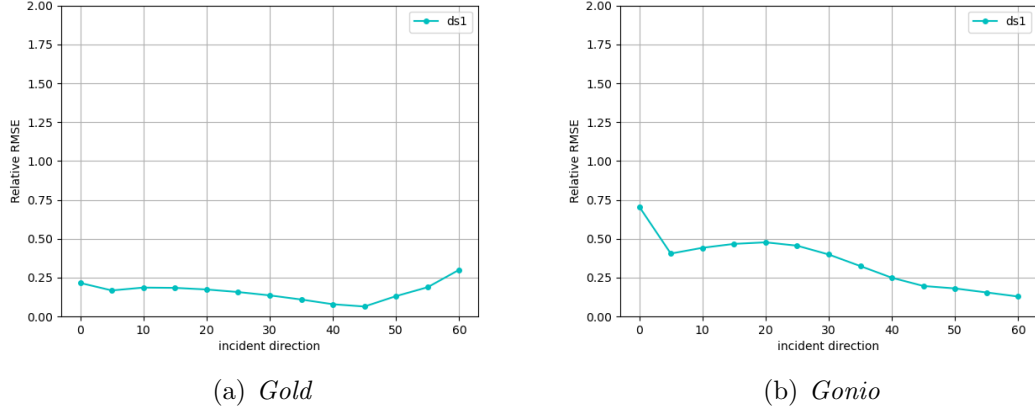


Figure 4.7: Relative RMSE errors as a function of incoming angle for GCMS data.

BRDFs show higher error with our estimates, but the values are nevertheless similar to that of Low et al. which involved 256x more samples. The obtained renderings further strengthen our case as there is hardly any difference between our and Low et al. estimates.

4.2 Neural latent space

The network from Fan et al. [7], discussed in Section 2.2.2, is a viable alternative to using physics-based parametric models. Being trained on a vast dataset of material BRDFs injects a strong prior in their network. Once trained, a set of directions with their corresponding BRDF values can be used to optimize the

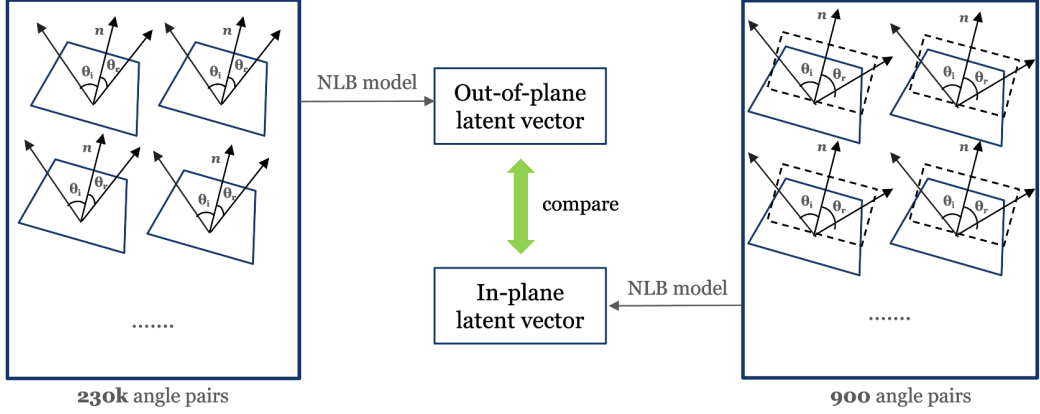


Figure 4.8: Schematic for our in-plane vs out-of-plane fitting pipeline using the NLB network.

latent vector for the material. As a rule of thumb, more data leads to better optimization. This provides an opportunity for us to test out the results using in-plane angles from both the packaging and MERL datasets. Since the network itself isn't restricted to in-plane predictions, we can use it to render materials for a visual comparison. Subsequently, optimizing the latent vector on Low et al. [6] angles will allow us to compare between the two. Overview provided in Figure 4.8.

The angles considered are the same as those of the parametric case (see Table 4.1). This also holds true for the parameterization, which is discussed in Section 4.1.2. The fitting, however, is different and follows the original paper by Fan et al. [7]. An exponential learning rate decay is followed, and an L1 loss is used between the network output and the ground truth BRDF values to optimize the latent vector.

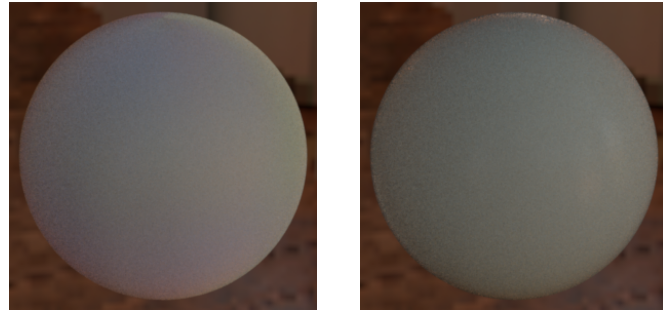
4.2.1 Results

For the renderings, a custom Mitsuba 3 [5] plugin is built to query BRDFs through the network. We follow the phong importance sampling routine to reduce variance. Due to certain implementation challenges owing to a lack of a GPU with high enough memory, we were unable to accommodate the NLB framework into the Mitsuba pipeline from Section 4.1.3. However, the comparisons between NLB



(a) Tungsten, [6]

(b) Tungsten, In-plane

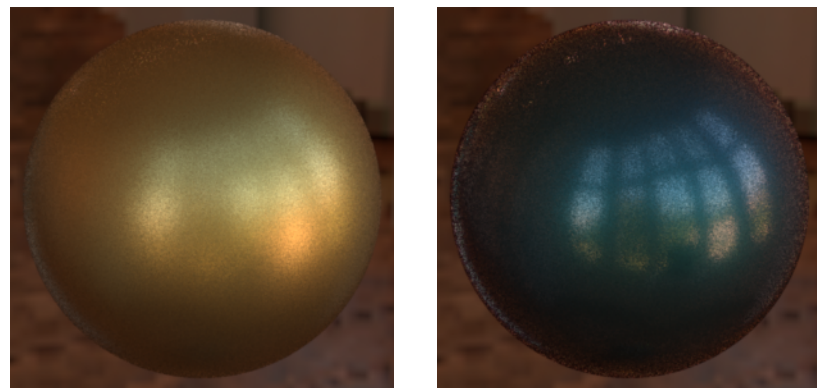


(c) Nylon, [6]

(d) Nylon, In-plane

Figure 4.9: Scene renderings for visual comparison. Notice the increased variance due to a naive importance sampling routine.

using Low et al. angles and NLB using in-plane angles are valid as we follow a consistent rendering pipeline. Shown in Figure 4.9 are side-by-side rendering comparisons for two MERL materials. Similarly, renderings for packaging materials are provided in Figure 4.10.



(a) Gold

(b) Gonio

Figure 4.10: Scene renderings for our packaging print materials, *Gold* and *Gonio*. These renderings are for in-plane data with only 900 samples.

We then move to the visual plots. BRDFs for chosen incoming angles are plot-

ted alongside their network predictions as a function of the outgoing angles. This is done for both MERL (Figure 4.11) and packaging print materials (Figure 4.12). It is evident that the network is able to track the ground truth data well, even using just the in-plane angle. Surprisingly, the Low et al. estimate seems to collapse for the Nylon material, being unable to watch the specular peak. This could be due to data imbalance stemming from a large number of samples lying around the diffuse region.

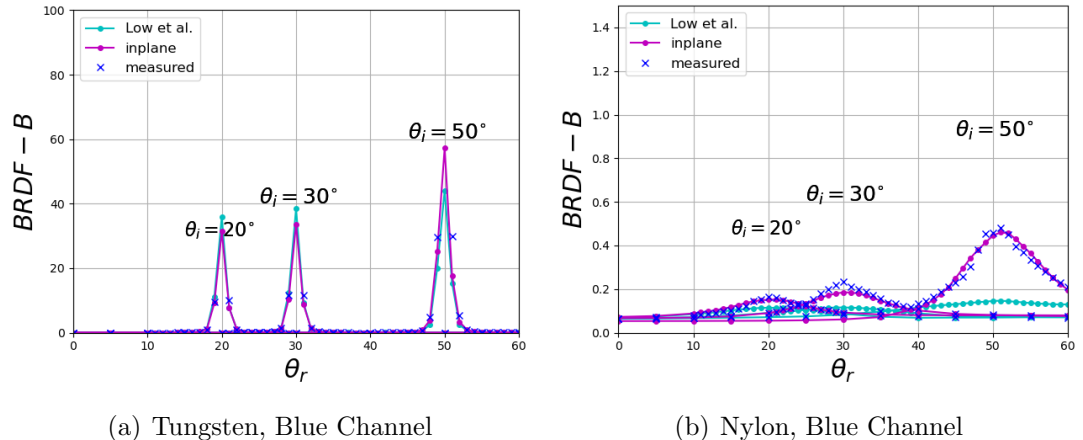


Figure 4.11: BRDF of MERL materials calculated with only in-plane data estimates compared to the estimates from [6] compared to the actual measurements.

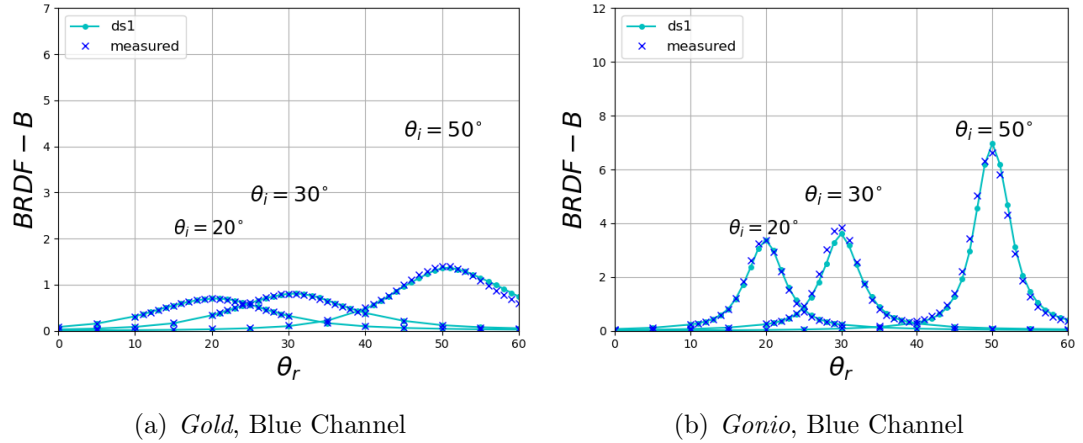


Figure 4.12: Contrasting fitted data with measured BRDF data of two packaging print materials.

Further analysis can be performed from relative-rmse error (Equation 4.3) plots as a function of the incident angle (Figures 4.13 and 4.14). For the various

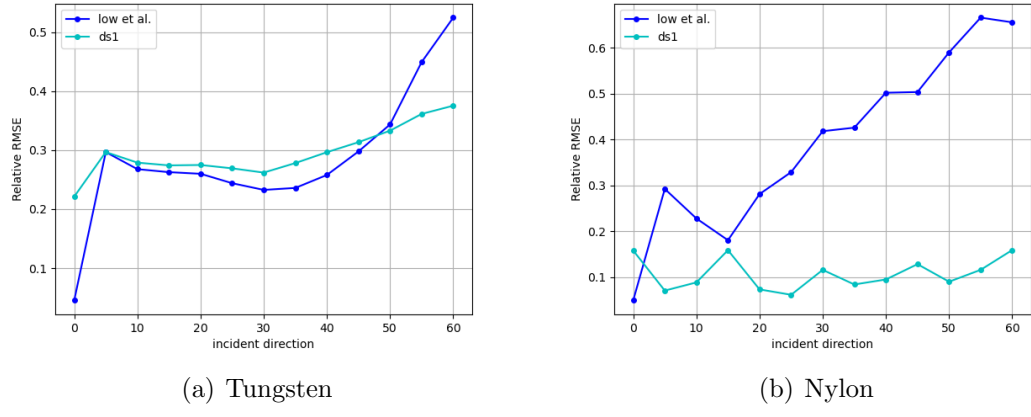


Figure 4.13: Relative RMSE errors as a function of incident angle for two MERL materials.

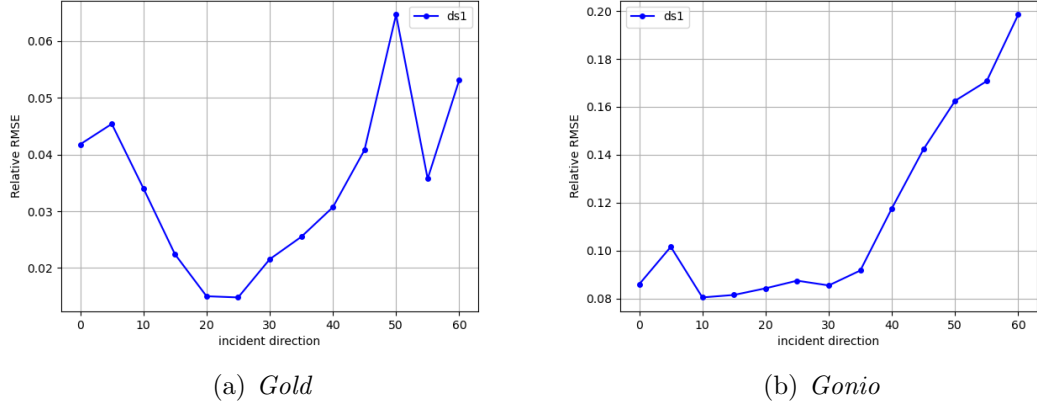


Figure 4.14: Relative RMSE errors as a function of incident angle for GCMS data.

materials we tried, both in-plane and out-of-plane estimates gave comparable error readings with no consistent trend, showing that in-plane parameters produce estimates that are just as good.

Overall, it is evident that both physics-based and network-based approaches do well with a fraction of the originally considered fitting data. This can help reduce acquisition times.

Chapter 5

Spectral representation

While tristimulus data is more readily available, and commonly used parametric models are more often than not in the RGB domain, it is still worth noting that the RGB color gamut is restricted. Moving down to RGB from spectral involves a wavelength compression step (shown in Section 2.2), leading to loss of information. It would be helpful to have representations that deal in the spectral space itself, thus removing the need for any premature spectral gamut compression. We propose a shallow multi-layer perceptron (MLP) to act as a compact and accurate BRDF representation.

5.1 MLP model

BRDF data consists of self-repeating patterns such as specular peaks. A neural network equipped with sufficient data should be able to exploit these patterns to learn the underlying BRDF and provide accurate estimates for unseen data points. This would help reduce the required number of measurements.

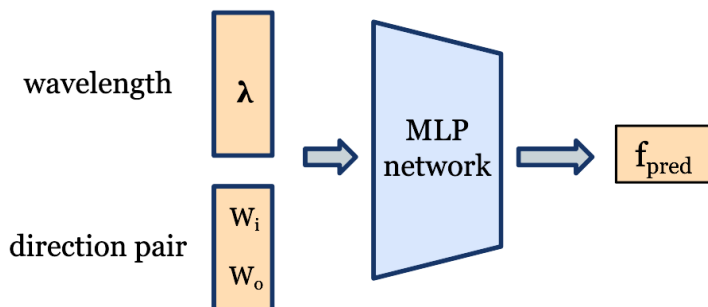


Figure 5.1: Schematic for our spectral BRDF network.

Figure 5.1 shows our MLP along with its input and output configurations. There are three hidden layers, each consisting of 10 nodes. This network design

Dataset	Incoming angles (θ_i°)
Test	$\{-50^\circ, -35^\circ, -20^\circ, -5^\circ, 10^\circ, 25^\circ, 40^\circ, 55^\circ\}$
Train	Angles at $5^\circ \in [-60^\circ, 60^\circ]$ excluding angles in Test

Table 5.1: Consideration of angles used to train the ANN.

was chosen after experimenting with several architectures. The packaging materials from Section 3.2 are arranged in input data triplets of incoming angle, outgoing angle, and wavelength. The input data, along with ground truth BRDF values, was split into a training and a test set to ensure fair performance evaluation on unseen data. This data split was performed as per Table 5.1. Incoming angles were segregated between the two splits, and all the outgoing angles for every wavelength were clubbed under the same split. A normalization is performed to improve model convergence before feeding in the input data. The output from the network is compared against the measured BRDF to propagate error gradients.

5.1.1 Network training

We use an exponential weighted Mean Squared Error (MSE) loss shown in Equation 5.1. This is to ensure that higher weights get assigned to specular data, driving the network to better capture the peaks.

$$L_{\text{MLP}} = \frac{1}{N} \sum_{n=1}^N e^{-\gamma|\theta_i^\circ - \theta_o^\circ|} \cdot (f_{\text{mea}} - f_{\text{pred}})^2 \quad (5.1)$$

f_{mea} is the measured BRDF, f_{pred} is the output from the MLP. θ_i and θ_o are the incoming and outgoing directions in degrees. The scaling is handled by the γ parameter. For our experiments, we used a γ value of 3, but we would suggest increasing it for materials with higher specular nature. For training, an ADAM optimiser was used with a decaying learning rate. We let the model train for 30 epochs and use the test data split to evaluate its performance on unseen data. This helps us choose the best-performing checkpoint.

5.1.2 Results

The results of our MLP model are presented through visual BRDF and quantitative error plots. For the BRDF plots, we pick 7 wavelengths out of the 31 and compare our measurements with the predictions for a chosen incoming angle. Figure 5.2 plots this for the *Gold* packaging material. It is evident that network predictions are able to track the measurements well for the most part, although there is some visible deviation around the specular peak.

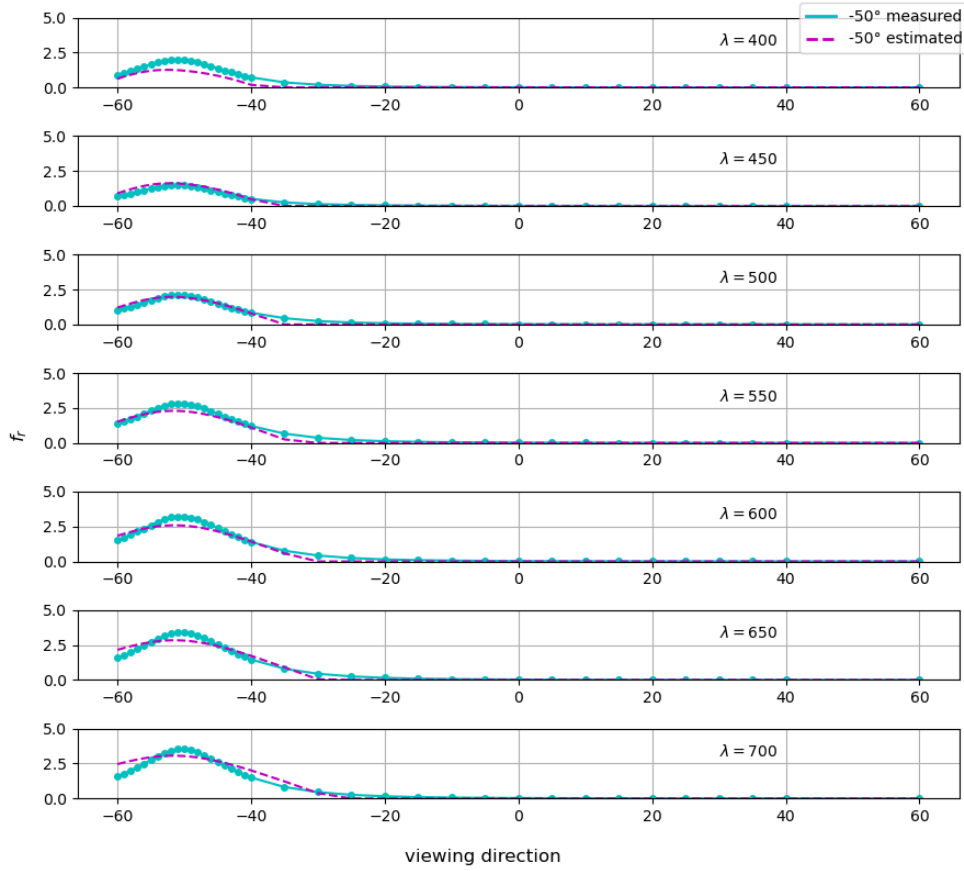


Figure 5.2: Measured and predicted spectral BRDF for seven wavelengths of the *Gold* packaging material.

To check for relative-rmse (same as Equation 4.3) across the spectrum, we generate a boxplot corresponding to individual wavelength (see Figure 5.3).

For a particular wavelength, each datapoint is an average relative-rmse error across an incoming angle for several outgoing angles. This is plotted alongside the average BRDF value for the wavelength, giving us an estimate of the prediction range. Here again, similar to the tristimulus loss, we only consider the glossy

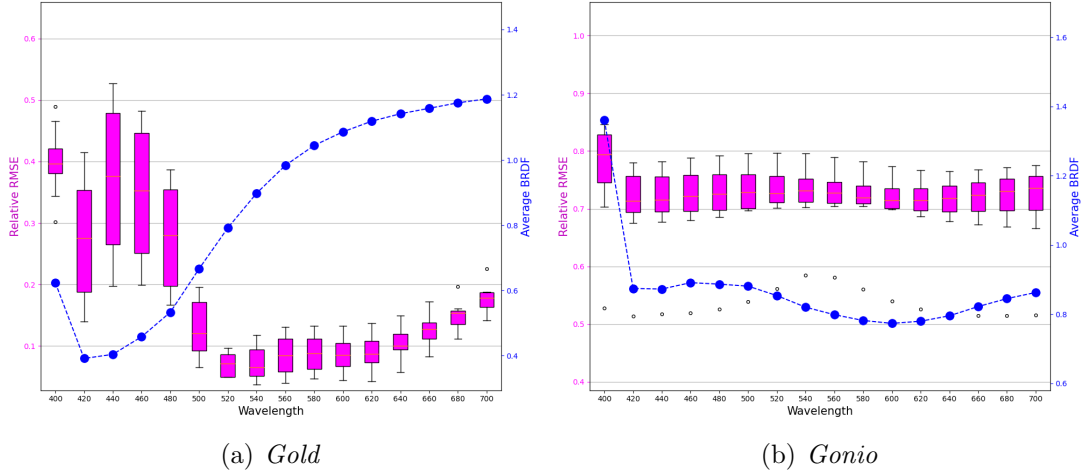


Figure 5.3: Box-and-whisker plots showing relative RMSE for *Gold* (left) and *Gonio* (right) across wavelengths.

angles, which we define as angles where incident and reflected directions are at most 10° apart. We restrict ourselves to using the test split for calculating relative-rmse for fairness.

These results show that a shallow MLP is capable of representing spectral BRDF data. This helps prevent us from having to do the gamut compression step and stick to the spectral domain if we like.

Chapter 6

Ablation studies

The experiments up until now show that, in the RGB domain, it is possible to use in-plane measurements for model fitting and generate renderings that closely resemble full gamut estimations. In the spectral domain, a compact neural network representation is able to learn from training data and capture BRDF trends, allowing it to make good estimates for unseen angles. However, it is important to check how little data is really required for our representations to be adequate.

We generate reduced datasets from the original in-plane data in Table 4.1. These are used to perform parameter estimations for the ABC model and latent vector optimization for the NLB network. We vary the number of datasets from DS1, the full in-plane dataset consisting of 900 direction pairs, to DS4, with 6 pairs. The angles considered are provided in Tables 6.1 and 6.2.

6.1 ABC method

We provide results similar to those in earlier chapters. Figure 6.1 provides renderings for the MERL materials with the ABC parameter fits on the reduced datasets. Similar renderings are also made available for the packaging print materials in Figure 6.2. It is evident that up until DS3-DS4, the plots look visually

Dataset	θ_i interval	θ_r interval: Diffuse	θ_r interval: Glossy
DS1	5°	5°	1°
DS2	15°	10°	2°
DS3	30°	20°	3°

Table 6.1: Angle intervals for the reduced fitting data (DS2-DS3).

Dataset	Incoming angle (θ_i°)	Outgoing angle (θ_r°)
DS4	30°	-60°, -20°, 20°, 28°, 36°, 60°

Table 6.2: Incoming and outgoing angles for the DS4 reduced dataset. Only **six** measurements are used.

consistent, with packaging print materials even showing good renderings with DS4, i.e. with six angle pairs. MERL materials, being steeper, perform worse with small data.

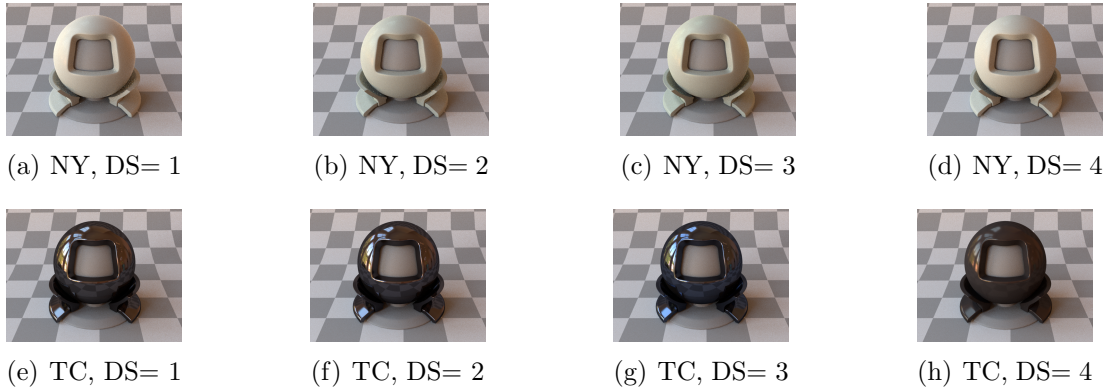


Figure 6.1: Scene renderings for visual comparison between parameters obtained with reduced in-plane datasets (DS1-DS4) on MERL materials. NY, and TC are Nylon, and Tungsten Carbide, respectively.

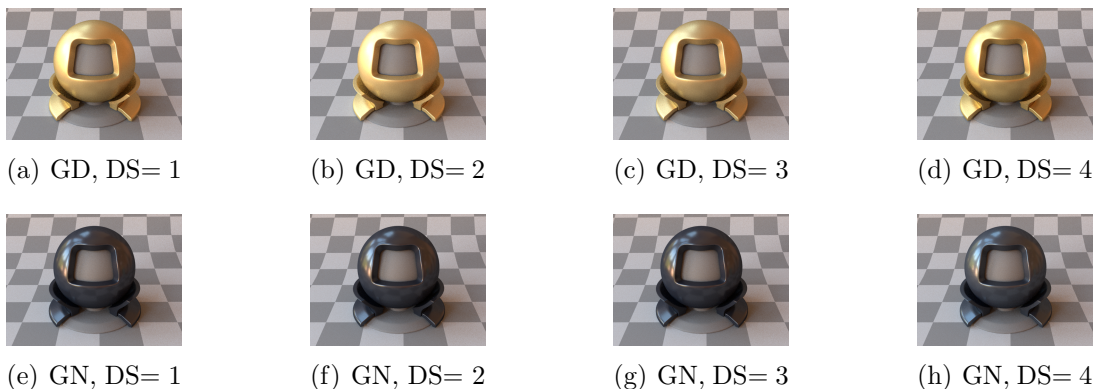


Figure 6.2: Scene renderings for visual comparison between parameters obtained for different in-plane datasets on our measured materials. GD, GN, are *Gold*, and *Gonio*, respectively.

Figures 6.3 and 6.4 show visual BRDF plots for MERL and packaging materials with the ABC method, and Figures 6.5 and 6.6 show their respective relative-rmse box-plots. As was hinted by the renderings, packaging material

estimates track the captured measurements better and produce a much lower relative-rmse. The boxplots also suggest that the error increases as we reduce the number of data points. With MERL, however, a clear trend is not visible. The reduced datasets still do pretty well overall, with better performance on the more diffuse Nylon than Tungsten carbide. These results suggest that we don't always need dense measurements to reproduce material BRDF, and for materials with smaller specular peaks, just a handful of measurements are enough.

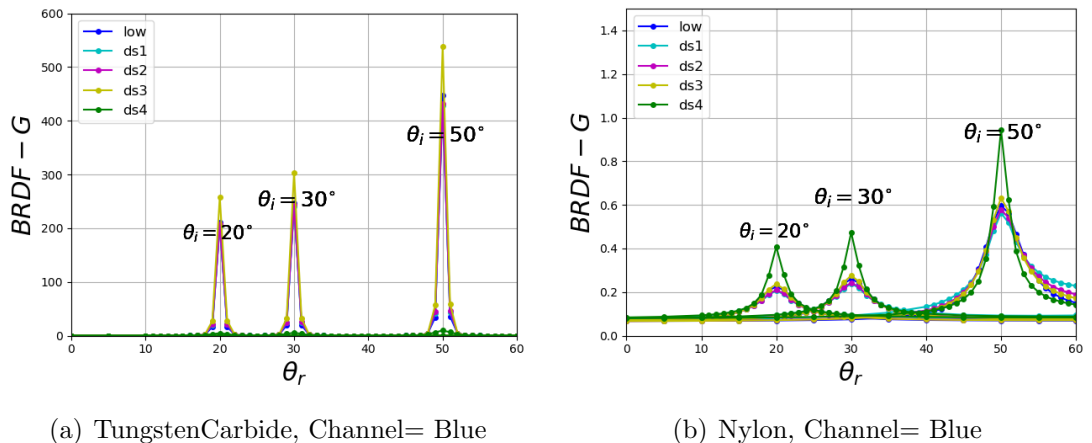


Figure 6.3: Parametrically calculated BRDF of MERL materials across reflected directions.

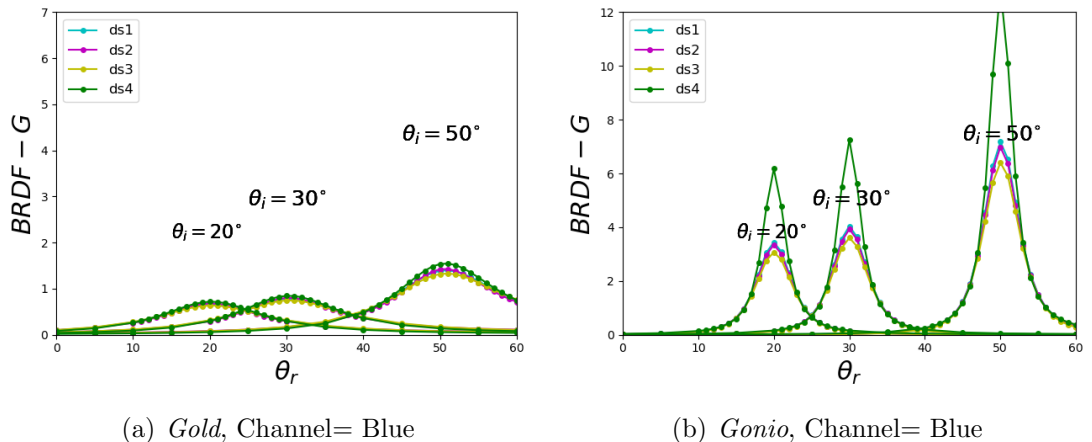


Figure 6.4: Parametrically calculated BRDF of our packaging materials across reflected directions.

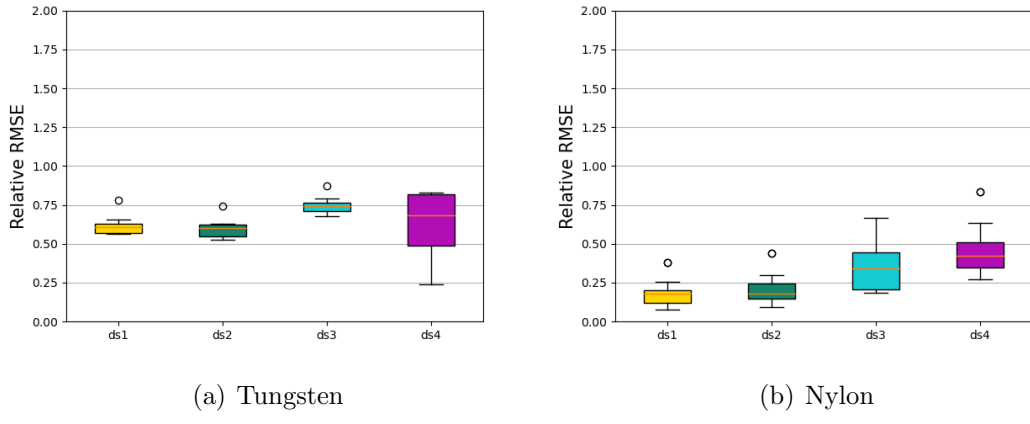


Figure 6.5: Box-and-whisker plots showing relative RMSE calculated using Equation 4.3 for the MERL materials TungstenCarbide and Nylon.

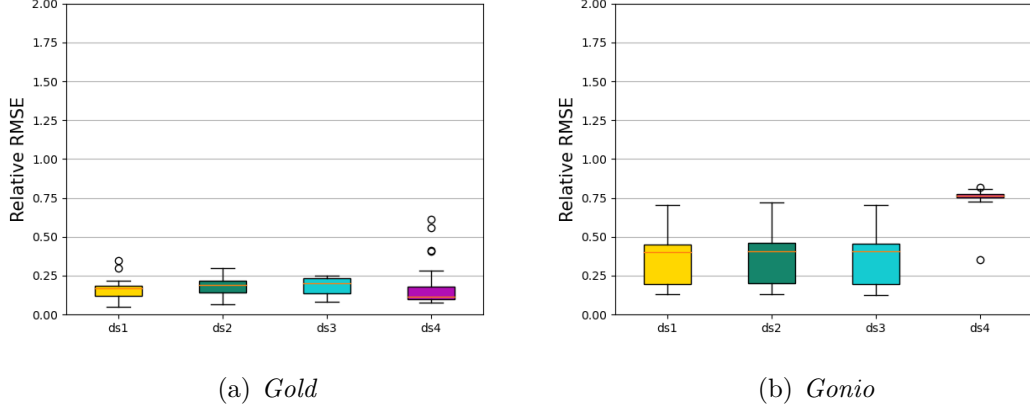


Figure 6.6: Box-and-whisker plots showing relative RMSE calculated using Equation 4.3 for the packaging print materials *Gold* and *Gonio*.

6.2 NLB method

We can generate equivalent plots by using the reduced datasets provided in Tables 6.1 and 6.2 for optimizing the latent vector on the trained NLB network. The rest of the pipeline stays the same and once optimized, the latent vector is used along with the network to generate following results.

We render the same scene from Section 4.2.1. The rendering plots for MERL and packaging materials are provided in Figures 6.7 and 6.8, respectively.

BRDF values are similarly tracked alongside the true measurements for datasets DS1-DS4 (Figures 6.9 and 6.10). Overall, the results seem better than those with

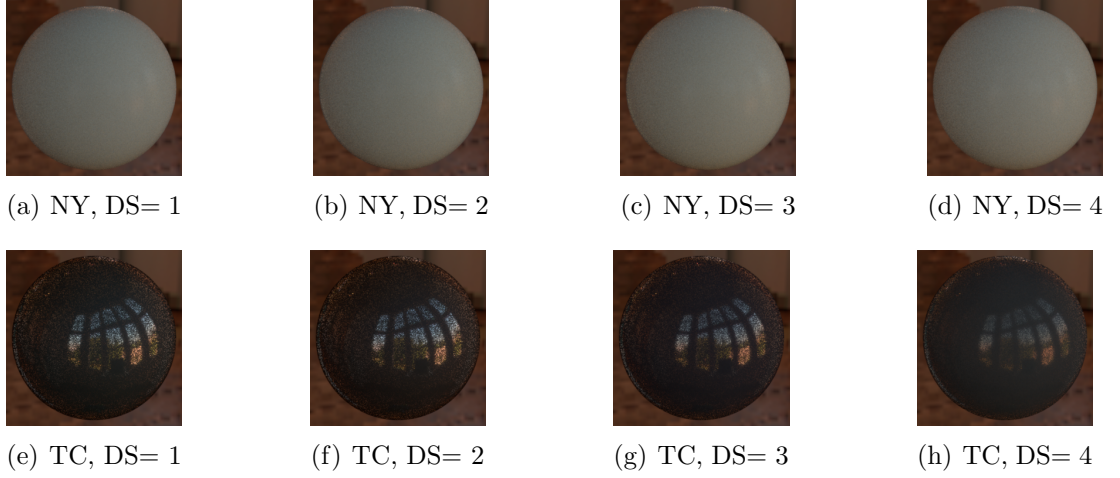


Figure 6.7: Scene renderings for visual comparison between reduced in-plane datasets (DS1-DS4) for MERL materials. NY, and TC are Nylon, and Tungsten Carbide, respectively.

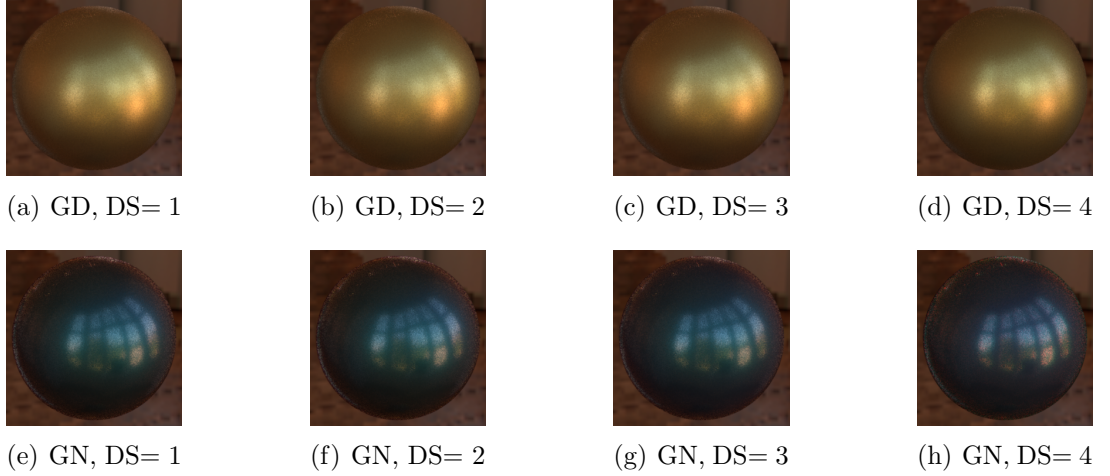


Figure 6.8: Scene renderings for visual comparison between reduced in-plane datasets on our measured materials. GD, GN, are *Gold*, and *Gonio*, respectively.

the ABC method. DS4 is primarily where the predictions start to deviate by a larger margin. Also, for the very steep Tungsten carbide material, the network is unable to predict the tip of the specular peak. We believe this response is due to the nature of the value resembling that of an outlier.

A better comparison can be made through relative-rmse boxplots shown in Figures 6.11 and 6.12. An obvious increase in error is seen with the reduction in fitting data. However, the error values are significantly lesser with NLB compared to the ABC parametric model.

Again, we land on a result similar to the ABC method. Due to the cumber-

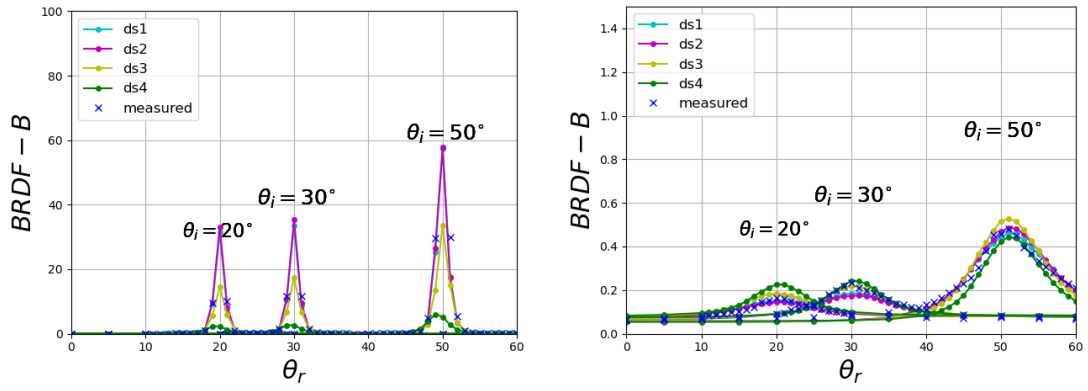


Figure 6.9: NLB network predictions of BRDF of MERL materials across outgoing directions.

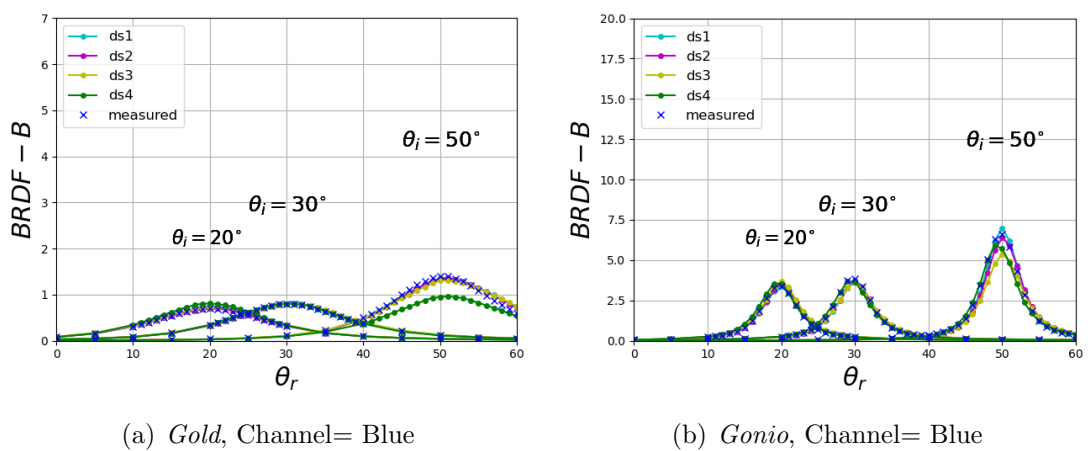


Figure 6.10: NLB network predictions of BRDF of our packaging materials across outgoing directions.

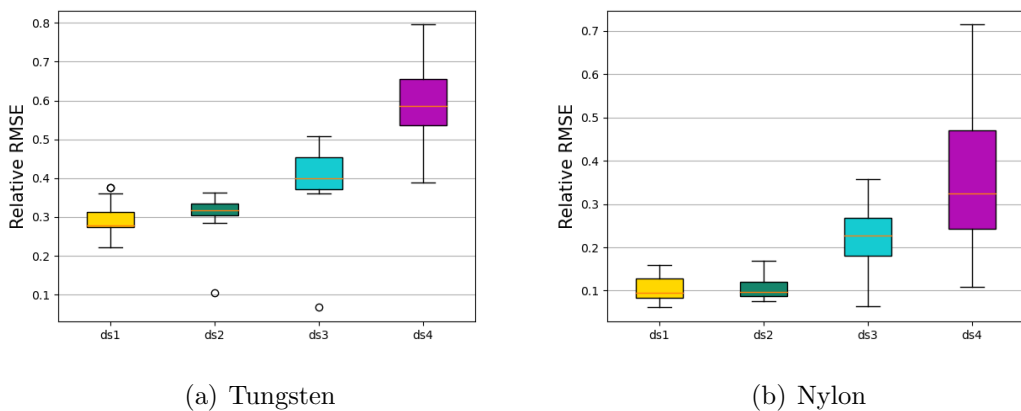


Figure 6.11: Box-and-whisker plots showing relative RMSE calculated using Equation 4.3 for the MERL materials Tungsten carbide and Nylon.

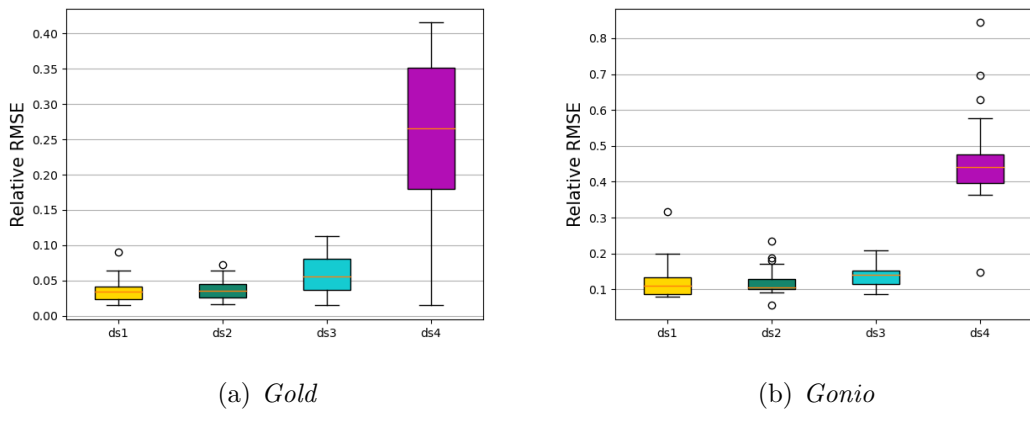


Figure 6.12: Box-and-whisker plots showing relative RMSE calculated using Equation 4.3 for the packaging print materials *Gold* and *Gonio*.

some training that the network underwent with hundreds of materials, we don't really need a vast number of samples to accurately match our material BRDF. Our reduced in-plane datasets performed well for the chosen materials, with only highly specular materials requiring hundreds of data points.

Chapter 7

Conclusion and future work

In this report, we have demonstrated the use of three separate representations for handling in-plane material BRDFs. This includes an MLP network specific to the spectral domain. This is important since most of the commonly seen representations lie in the tristimulus gamut. Similarly, we show that existing microfacet-based and network-based parametric models can work with in-plane data to generate their parametric estimates. We find in-plane estimates to be a fair approximation of the ones derived using substantially more angular samples. These parametric models also circumvent the issue regarding the inability to render solely using in-plane BRDF data. We report our results both visually through 3d renderings and quantitatively through BRDF and relative-rmse plots.

Renderings generated using in-plane estimates are virtually indistinguishable from those using more data. This is more so true for materials with gentle specular peaks, i.e., a more diffuse nature. As the specular peak starts getting steeper, we usually run into an issue with the models being unable to capture the tip of the peak. This can be somewhat helped by using losses that are lenient with outliers, such as the L1 loss. Moreover, our results only hold true for isotropic materials as in-plane results stay consistent when changing the azimuthal angles (keeping the difference constant). This is not true for anisotropic materials, for whom a more nuanced approach needs to be developed. We leave this for future work. Aside from anisotropic materials, there is scope for future study in representing materials that are more complex such as spatially varying materials and layered materials. In Appendix A, we have provided a literature survey of sorts to identify existing works handling such materials. This can act as a good starting point for

getting accustomed to them.

Nevertheless, we believe that our results can help reduce BRDF acquisition times by allowing users to measure a fraction of the direction pairs. What fraction to consider is a function of the user requirements, and through our experiment we have shown how the results vary on varying the number of data points.

REFERENCES

- [1] U. S. N. B. of Standards and F. E. Nicodemus, *Geometrical considerations and nomenclature for reflectance*. US Department of Commerce, National Bureau of Standards Washington, DC, USA, 1977, vol. 160.
- [2] D. Guarnera, G. C. Guarnera, A. Ghosh, C. Denk, and M. Glencross, “BRDF representation and acquisition,” in *Computer Graphics Forum*, vol. 35, no. 2. Wiley Online Library, 2016, pp. 625–650.
- [3] R. L. Cook and K. E. Torrance, “A reflectance model for computer graphics,” *ACM Transactions on Graphics (ToG)*, vol. 1, no. 1, pp. 7–24, 1982.
- [4] J. Dupuy and W. Jakob, “An adaptive parameterization for efficient material acquisition and rendering,” *ACM Transactions on graphics (TOG)*, vol. 37, no. 6, pp. 1–14, 2018.
- [5] W. Jakob, S. Speierer, N. Roussel, M. Nimier-David, D. Vicini, T. Zeltner, B. Nicolet, M. Crespo, V. Leroy, and Z. Zhang, “Mitsuba 3 renderer,” 2022, <https://mitsuba-renderer.org>.
- [6] J. Löw, J. Kronander, A. Ynnerman, and J. Unger, “BRDF models for accurate and efficient rendering of glossy surfaces,” *ACM Transactions on Graphics (TOG)*, vol. 31, no. 1, pp. 1–14, 2012.
- [7] J. Fan, B. Wang, M. Hasan, J. Yang, and L.-Q. Yan, “Neural layered brdfs,” in *ACM SIGGRAPH 2022 Conference Proceedings*, 2022, pp. 1–8.
- [8] W. Matusik, H. Pfister, M. Brand, and L. McMillan, “A data-driven reflectance model,” *ACM Transactions on Graphics (TOG)*, vol. 22, no. 3, pp. 759–769, 2003.
- [9] A. Sole, G. C. Guarnera, I. Farup, and P. Nussbaum, “Measurement and rendering of complex non-diffuse and goniochromatic packaging materials,” *The Visual Computer*, vol. 37, no. 8, pp. 2207–2220, 2021.
- [10] J. Palmer and B. G. Grant, *The Art of Radiometry*. SPIE Press Bellingham, Washington USA, 2010, no. ISBN 978-0-8194-7245-8.
- [11] D. A. Kerr, “The cie xyz and xyy color spaces,” *Colorimetry*, vol. 1, no. 1, pp. 1–16, 2010.

- [12] C. IEC, “61966-2-1: 1999: Multimedia systems and equipment—colour measurement and management—part 2-1: Colour management—default rgb colour space—srgb,” *CIE: Vienna, Austria*, 1999.
- [13] B. Hu, J. Guo, Y. Chen, M. Li, and Y. Guo, “DeepBRDF: A deep representation for manipulating measured BRDF,” in *Computer Graphics Forum*, vol. 39, no. 2. Wiley Online Library, 2020, pp. 157–166.
- [14] A. Sztrajman, G. Rainer, T. Ritschel, and T. Weyrich, “Neural brdf representation and importance sampling,” in *Computer Graphics Forum*, vol. 40, no. 6. Wiley Online Library, 2021, pp. 332–346.
- [15] G. Rainer, W. Jakob, A. Ghosh, and T. Weyrich, “Neural BTF compression and interpolation,” in *Computer Graphics Forum*, vol. 38, no. 2. Wiley Online Library, 2019, pp. 235–244.
- [16] G. Rainer, A. Ghosh, W. Jakob, and T. Weyrich, “Unified neural encoding of BTFs,” in *Computer graphics forum*, vol. 39, no. 2. Wiley Online Library, 2020, pp. 167–178.
- [17] A. Kuznetsov, “NeuMIP: Multi-resolution neural materials,” *ACM Transactions on Graphics (TOG)*, vol. 40, no. 4, 2021.
- [18] C. Liu, M. Fischer, and T. Ritschel, “Learning to learn and sample brdfs,” in *Computer Graphics Forum*, vol. 42, no. 2. Wiley Online Library, 2023, pp. 201–211.
- [19] V. Deschaintre, M. Aittala, F. Durand, G. Drettakis, and A. Bousseau, “Single-image svbrdf capture with a rendering-aware deep network,” *ACM Transactions on Graphics (ToG)*, vol. 37, no. 4, pp. 1–15, 2018.
- [20] X. Zhou and N. K. Kalantari, “Adversarial single-image svbrdf estimation with hybrid training,” in *Computer Graphics Forum*, vol. 40, no. 2. Wiley Online Library, 2021, pp. 315–325.
- [21] S. Sang and M. Chandraker, “Single-shot neural relighting and svbrdf estimation,” in *Computer Vision–ECCV 2020: 16th European Conference, Glasgow, UK, August 23–28, 2020, Proceedings, Part XIX 16*. Springer, 2020, pp. 85–101.
- [22] J. Bieron, X. Tong, and P. Peers, “Single image neural material relighting,” in *ACM SIGGRAPH 2023 Conference Proceedings*, 2023, pp. 1–11.
- [23] J. Fan, B. Wang, M. Hasan, J. Yang, and L.-Q. Yan, “Neural biplane representation for btf rendering and acquisition,” in *ACM SIGGRAPH 2023 Conference Proceedings*, 2023, pp. 1–11.

- [24] E. P. Lafourne, S.-C. Foo, K. E. Torrance, and D. P. Greenberg, “Non-linear approximation of reflectance functions,” in *Proceedings of the 24th annual conference on Computer graphics and interactive techniques*, 1997, pp. 117–126.
- [25] A. Ngan, F. Durand, and W. Matusik, “Experimental analysis of brdf models.” *Rendering Techniques*, vol. 2005, no. 16th, p. 2, 2005.
- [26] A. Weidlich and A. Wilkie, “Arbitrarily layered micro-facet surfaces,” in *Proceedings of the 5th international conference on Computer graphics and interactive techniques in Australia and Southeast Asia*, 2007, pp. 171–178.
- [27] W. Jakob, E. d’Eon, O. Jakob, and S. Marschner, “A comprehensive framework for rendering layered materials,” *ACM Transactions on Graphics (ToG)*, vol. 33, no. 4, pp. 1–14, 2014.
- [28] T. Zeltner and W. Jakob, “The layer laboratory: a calculus for additive and subtractive composition of anisotropic surface reflectance,” *ACM Transactions on Graphics (TOG)*, vol. 37, no. 4, pp. 1–14, 2018.
- [29] L. Belcour, “Efficient rendering of layered materials using an atomic decomposition with statistical operators,” *ACM Transactions on Graphics*, vol. 37, no. 4, p. 1, 2018.
- [30] P. Weier and L. Belcour, “Rendering layered materials with anisotropic interfaces,” *Journal of Computer Graphics Techniques (JCGT)*, vol. 9, no. 2, p. 20, 2020.
- [31] T. Yamaguchi, T. Yatagawa, Y. Tokuyoshi, and S. Morishima, “Real-time rendering of layered materials with anisotropic normal distributions,” in *SIGGRAPH Asia 2019 Technical Briefs*, 2019, pp. 87–90.
- [32] Y. Guo, M. Hašan, and S. Zhao, “Position-free monte carlo simulation for arbitrary layered bsdfs,” *ACM Transactions on Graphics (ToG)*, vol. 37, no. 6, pp. 1–14, 2018.
- [33] E. Veach, *Robust Monte Carlo methods for light transport simulation*. Stanford University, 1998.
- [34] H. P. Lensch, J. Kautz, M. Goesele, W. Heidrich, and H.-P. Seidel, “Image-based reconstruction of spatial appearance and geometric detail,” *ACM Transactions on Graphics (TOG)*, vol. 22, no. 2, pp. 234–257, 2003.
- [35] P. Debevec, T. Hawkins, C. Tchou, H.-P. Duiker, W. Sarokin, and M. Sagar, “Acquiring the reflectance field of a human face,” in *Proceedings of the 27th annual conference on Computer graphics and interactive techniques*, 2000, pp. 145–156.

- [36] X. Li, Y. Dong, P. Peers, and X. Tong, “Modeling surface appearance from a single photograph using self-augmented convolutional neural networks,” *ACM Transactions on Graphics (ToG)*, vol. 36, no. 4, pp. 1–11, 2017.
- [37] X. Zhou and N. K. Kalantari, “Look-ahead training with learned reflectance loss for single-image svbrdf estimation,” *ACM Transactions on Graphics (TOG)*, vol. 41, no. 6, pp. 1–12, 2022.
- [38] J. Guo, S. Lai, C. Tao, Y. Cai, L. Wang, Y. Guo, and L.-Q. Yan, “Highlight-aware two-stream network for single-image svbrdf acquisition,” *ACM Transactions on Graphics (TOG)*, vol. 40, no. 4, pp. 1–14, 2021.
- [39] G. Vecchio, S. Palazzo, and C. Spampinato, “Surfacenet: Adversarial svbrdf estimation from a single image,” in *Proceedings of the IEEE/CVF International Conference on Computer Vision*, 2021, pp. 12 840–12 848.
- [40] G. Vecchio, R. Martin, A. Roullier, A. Kaiser, R. Rouffet, V. Deschaintre, and T. Boubekeur, “Controlmat: A controlled generative approach to material capture,” *arXiv preprint arXiv:2309.01700*, 2023.
- [41] X. Zhou, M. Hasan, V. Deschaintre, P. Guerrero, Y. Hold-Geoffroy, K. Sunkavalli, and N. K. Kalantari, “Photomat: A material generator learned from single flash photos,” in *ACM SIGGRAPH 2023 Conference Proceedings*, 2023, pp. 1–11.
- [42] X. Zhou, M. Hasan, V. Deschaintre, P. Guerrero, K. Sunkavalli, and N. K. Kalantari, “Tilegen: Tileable, controllable material generation and capture,” in *SIGGRAPH Asia 2022 conference papers*, 2022, pp. 1–9.
- [43] J. Bieron, X. Tong, and P. Peers, “Single image neural material relighting,” in *ACM SIGGRAPH 2023 Conference Proceedings*, 2023, pp. 1–11.
- [44] D. Gao, X. Li, Y. Dong, P. Peers, K. Xu, and X. Tong, “Deep inverse rendering for high-resolution svbrdf estimation from an arbitrary number of images.” *ACM Trans. Graph.*, vol. 38, no. 4, pp. 134–1, 2019.

APPENDICES

A Beyond regular BRDFs

Throughout the report we have talked about isotropic materials. These form a small subset of the kind of materials we encounter in our everyday lives. In fact, we hardly ever come across materials this uniform. More often than not, real-world materials show more complex optical properties like anisotropy. Also, a vast range of objects are built with multiple materials, often layered on top of each other, as is the case with polished metals or varnish coatings. It is imperative to be able to handle such materials. Similarly, in this work, we have kept the BRDF function independent of the spatial position. This is a good approximation for certain materials that show a consistent optical nature, but for the most part, different positions interact with light differently. This is often modeled using a BRDF texture map, where each texel (element on the map) corresponds to BRDF parameters specific to a certain spatial location. This offers us more flexibility but also significantly increases the number of parameters that we have to deal with. In the following sections, we will go over how these materials are handled.

Layered BRDFs

There are countless examples of materials that comprise several layers to bring about more intricate light interactions. Metals are often coated with transparent or semi-transparent mediums to make them appear more polished. Decoration items such as vases use a similar concept to get a glass-like finish. Handling such materials is often difficult as the BRDF calculations concerning them are

analogous to materials showing subsurface scattering. This means as we increase the layers, we need to keep track of more and more ray trajectories within the material. It is possible to define the material arrangement geometrically in a scene, but letting the renderer handle such materials leads to poor results. This is similar to how tracing rays from the light isn't recommended as there aren't enough rays hitting the sensor. We need to treat such light interactions separately.

While multiple methods have been proposed in the past to handle layered materials, they either made several simplifying assumptions regarding the individual layers' BRDF nature, leading to poor performance and limited applicability or often didn't provide a means to sample PDFs for importance sampling. Also, a subset of these methods were entirely empirical. Weidlich and Wilkie [26] first proposed an approach that allowed flexible choice of layer BRDFs. Microfacet theory [3] was used to model the light transport within layers with certain simplifications to avoid subsurface computations. These were:

- To treat microfacet widths to be larger than layer widths.
- Rays were assumed to enter and exit from the same point. This was even considered true for layers refracted into the surface
- Scattering wasn't present within the layers and occurred only at the interface.

Modeling the light transport then led to a recursive equation that estimated the overall BRDF. They incorporated absorption and total internal reflection terms to factor in their contribution. For importance sampling, individual BRDF probabilities were suitably weighted to derive a PDF that followed the layered BRDF closely. Overall, the resulting model was compact, physically based, and fairly straightforward to implement and also covered a wider range of materials.

Works targeting the fourier directional basis were proposed next [27, 28] as they were much more accurate than existing methods. The tradeoff, however, was in terms of the expensive precomputation required. While [27] was restricted

to isotropic materials, the follow-up work [28] allowed for anisotropy, leading to a more general framework for handling layered materials. Their method was motivated by the *adding equations*, using which a surface illumination integral was derived at layer boundaries. A fourier series basis along the azimuthal angle was used to help solve this integral. This approach allows for choosing the phase function that models the scattering within layers. An importance sampling scheme was also proposed to reduce the resulting variance. [28] additionally talks about additive and subtractive composition of materials as operations in the directional space. Aside from the precomputations, these methods offer a more accurate means to tackle layered BRDFs with additional flexibility.

Belcour [29] bridged the gap between the above two methods, offering accuracy comparable to the fourier approaches while still being efficient like those modeling approximate light transport. This was followed up by two works [30, 31] allowing for anisotropy. The idea behind [29] was to think of the GGX BSDF lobes through directional statistics such as energy, mean, and variance. Belcour derived operators on the directional statistics by modeling or approximating the light transport phenomena (reflection, refraction, volume scattering, and absorption) empirically. Resultant BSDF lobes were aggregated using the adding-doubling method for plane-parallel media to get the material BSDF.

All of the works discussed above introduced approximations in some form or the other. Guo et al. [32] was the first unbiased model that relied on Monte Carlo simulations for light transport within layers. The only simplification considered was that the spatial extent is larger than the layer depth, allowing for a parameterization only along the depth. What follows is a modification of the path integral formulation of Veach [33] for the depth parameterization and proposing strategies for sampling these paths along with their BSDF and PDF estimation. Not only does the method further allow for more flexibility in the form of normal mapping, anisotropy, and spatial variation, but the framework is also suitable for bidirectional path tracing and multiple importance sampling. An approximation

with a small bias is also provided to speed up the rendering.

The work Neural layered BRDFs [7] follows Guo et al. [32] results as a ground truth for model training. Apart from the representation network discussed in Section 2.2.2, a layering network is used to perform material layering in the latent space, where given two input material latent vectors (V_{top} and V_{bottom}) and parameters for the medium in between them (albedo A and extinction coefficient σ_T), the layering network (g_2) outputs a latent vector (V_{layered}) equivalent to the input material configuration (Equation A.1).

$$g_2(V_{\text{top}}, V_{\text{bottom}}, A, \sigma_T) = V_{\text{layered}} \quad (\text{A.1})$$

This deterministic learning allows the network to produce nearly perfect results without going over the Monte Carlo simulation process, saving further time and eliminating any variance introduced via Monte Carlo.

The several methods discussed here form a formidable toolbox to deal with layered materials. The choice of the model rests on the user and their particular application, with certain use cases requiring efficient renderings while others focusing more on the photorealism aspect.

Spatially varying BRDFs

Another class of materials that we are more likely to view are those with spatially varying properties. Either by design or imperfections during fabrication, it is common to see different spatial locations of the same object showing contrasting behavior. These properties might either change gradually along the surface or show drastic variations. There are three kinds of approaches often used to deal with such materials, as discussed in [34]. The first is to get the BRDF data across multiple surface points and tabulate all of it. This is similar to how MERL [8] tabulates their BRDF measurements and interpolates them during rendering, just that here, the BRDF also acts as a function of the surface point being

considered. The existing issues with storage and material-specific nature when tabulating spatially invariant BRDFs are even more problematic as the data is substantially more. Another option is to use a light-field-like setup and query appropriate image slices to estimate reflectance values. However, this approach poses completely different issues related to light-field capture while still not eliminating the material-specific nature of data. The current standard for dealing with spatial materials is to treat them as BRDF texture maps. This allows us to partition the object surface into individual texels, each acting as an independent BRDF with its own BRDF parameters. Querying the BRDF then becomes an operation over these parameters, provided we have texel-specific incoming and outgoing light directions.

Some of the early works handling spatially varying materials were [34] and [35]. Debevec et al. [35] dealt specifically with human face reflectance maps and allowed for arbitrary variation of certain BRDF parameters across the skin surface while keeping others fixed. A more general method to handle materials was proposed by [34]. They required a few (15-25) high dynamic range images of the material surface, following which camera parameters were used to project the object mesh onto the image plane. Object points were identified across images, and Lafourte models were fitted onto them. To compensate for scarcity, clusters of similar materials were formed, and a basis of BRDF models was derived for each cluster. Within the cluster, every point was assigned a BRDF through a linear combination of this basis. This approach effectively segregated similar materials within the object and accounted for spatial variation within the clusters.

Although theoretically solid, the methods mentioned above often require a lot more information for capturing material BRDFs, such as the object mesh, camera parameters, and accurate lighting information. It is not always possible to get hold of certain details with *in-the-wild* images. This is where deep learning methods shine. It should be noted that going forward, we will restrict our focus to planar materials. There are separate methods that also deal with

geometry, but those won’t be covered here. Li et al. [36] devised one of the very first pipelines to estimate SVBRDF maps from single (synthetic) images using a convolutional neural network (CNN). Their manuscript also provides a detailed description of pre- deep learning methods to handle single-image reflectance modeling in the *Related Work* section. Deschaintre et al. [19] further paved the way for such SVBRDF capture methods by procedurally building a large synthetic dataset of realistic SVBRDF maps under diverse lighting and with diverse material types such as leather, metal, plastic, fabric, etc. Given an input image, their CNN architecture predicts a set of texture maps (normal, diffuse albedo, specular albedo, and specular roughness). The novelty of this method is also a rendering loss, wherein the estimated parameter maps are used to perform differentiable forward rendering, and the same is done with the ground-truth maps. A reconstruction loss is computed between the rendered images and is used to optimize the network. This loss computation is performed for multiple lighting and viewing configurations. Although their training relies on synthetic data, the network generates close estimates with real-world inputs.

After [19], several works targeting single-image SVBRDF capture were proposed [20, 37, 38, 39] utilizing techniques such as adversarial-learning (GANs) and meta-learning. Recently Vecchio et al. [40] used diffusion models to capture material SVBRDFs. Their framework also allows for conditioning over text or image prompts, providing additional control over the output. With the generative models, one can go a step ahead and learn the distribution over input material images rather than the BRDF maps. This would enable us to generate completely new materials. A recent work by Zhou et al. [41], which is a follow-up to [42] by the same authors, builds such a comprehensive framework comprised of a generator, a relighting module, and a maps estimator. The generator takes a latent vector input and produces material-specific features. Passing this to the relighting module with an input lighting configuration produces the image of the material under that specific lighting. An adversarial loss is used to compare be-

tween the relit image and a real image under the same lighting. Once both the generator and relighting module are trained, a maps estimator is introduced that takes the generator output and estimates the SVBRDF texture maps. To train the maps estimator, a rendering loss similar to [19] is used to compare forward renderings (from the texture maps) and outputs from the relighting module for diverse lighting conditions. The thing to note here is that this method doesn't rely on synthetic images and uses images captured through hand-held devices. Additionally, ground truth SVBRDF maps are not necessary.

Relighting is frequently brought up in SVBRDF literature. Estimating accurate SVBRDF texture maps allows us to generate realistic renderings for arbitrary light directions. The relighting module from [41] takes a different approach by solely relying on the material representations from the generator to produce relit images. Bieron et al. [43] also bypass predicting the intermediate texture maps and performing a forward rendering and instead generate the relighting results directly using a neural network. They further suggest that their relit images can enrich existing inputs and demonstrate a bump in performance with the inverse rendering framework of Gao et al. [44].

This concludes the study of single-image SVBRDF capture methods for planar materials. Their resulting texture maps are ready to be used by modern-day renderers. The power of these methods is that any of us can capture a digital copy of a material that we have come across by taking a single image, view it under a lighting of our choice, or even birth new materials from scratch.